

Naval Research Laboratory

Washington, DC 20375-5000



NRL Memorandum Report 6486

2

AD-A210 465

Numerical Simulation of the Compressible  
Orszag-Tang Vortex

R.B. DAHLBURG AND J.M. PICONE

*Laboratory for Computational Physics and Fluid Dynamics*

DTIC  
ELECTE  
JUL 21 1989  
S D

June 8, 1989

SECURITY CLASSIFICATION OF THIS PAGE

REPORT DOCUMENTATION PAGE				Form Approved OMB No 0704 0188	
1a REPORT SECURITY CLASSIFICATION <b>UNCLASSIFIED</b>			1b RESTRICTIVE MARKINGS		
2a SECURITY CLASSIFICATION AUTHORITY			3 DISTRIBUTION AVAILABILITY OF REPORT		
2b DECLASSIFICATION/DOWNGRADING SCHEDULE			Approved for public release; distribution unlimited.		
4 PERFORMING ORGANIZATION REPORT NUMBER(S)  NRL Memorandum Report 6486			5 MONITORING ORGANIZATION REPORT NUMBER(S)		
6a NAME OF PERFORMING ORGANIZATION  Naval Research Laboratory		6b OFFICE SYMBOL (If applicable)  Code 4440	7a NAME OF MONITORING ORGANIZATION		
6c ADDRESS (City, State, and ZIP Code)  Washington, DC 20375-5000			7b ADDRESS (City, State, and ZIP Code)		
8a NAME OF FUNDING/SPONSORING ORGANIZATION  NASA		8b OFFICE SYMBOL (If applicable)	9 PROCUREMENT INSTRUMENT IDENTIFICATION NUMBER		
8c ADDRESS (City, State, and ZIP Code)  Washington, DC 20546			10 SOURCE OF FUNDING NUMBERS		
			PROGRAM ELEMENT NO  W-16, 672	PROJECT NO  W-16m672	TASK NO  NASA
			WORK UNIT ACCESSION NO		
11 TITLE (Include Security Classification)  Numerical Simulation of the Compressible Orszag-Tang Vortex					
12 PERSONAL AUTHOR(S)  Dahlburg, R.B. and Picone, J.M.					
13a TYPE OF REPORT  Interim		13b TIME COVERED FROM 6/88 TO 2/89		14 DATE OF REPORT (Year, Month, Day)  1989 June 8	
15 PAGE COUNT  54					
16 SUPPLEMENTARY NOTATION					
17 COSATI CODES			18 SUBJECT TERMS (Continue on reverse if necessary and identify by block number)		
FIELD	GROUP	SUB-GROUP	Compressible magnetohydrodynamic turbulence solar wind structuring		
			Direct numerical simulation (code)		
19 ABSTRACT (Continue on reverse if necessary and identify by block number)  This paper presents the results of fully compressible, Fourier collocation, numerical simulations of the Orszag-Tang vortex system. The initial conditions for this system consist of a nonrandom, periodic field in which the magnetic and velocity fields contain X-points but differ in modal structure along one spatial direction. The velocity field is initially solenoidal, with the total initial pressure field consisting of the superposition of the appropriate incompressible pressure distribution upon a flat pressure field corresponding to the initial, average, Mach number of  (Continues)					
20 DISTRIBUTION/AVAILABILITY OF ABSTRACT <input checked="" type="checkbox"/> UNCLASSIFIED/UNLIMITED <input type="checkbox"/> SAME AS RPT <input type="checkbox"/> DTIC USERS			21 ABSTRACT SECURITY CLASSIFICATION  UNCLASSIFIED		
22a NAME OF RESPONSIBLE INDIVIDUAL  R.B. Dahlburg			22b TELEPHONE (Include Area Code)  (202) 767-0808		22c OFFICE SYMBOL  Code 4440

DD Form 1473, JUN 86

Previous editions are obsolete

S/N 0102-LF-014-6603

SECURITY CLASSIFICATION OF THIS PAGE

## 19. ABSTRACTS (Continued)

the flow. In our numerical simulations, we vary this initial Mach number from 0.2 to 0.6. These values correspond to average plasma  $\beta$  values ranging from 30.0 to 3.3, respectively. We find that compressible effects develop within one or two Alfvén transit times, as manifested in the spectra of compressible quantities such as the mass density and the nonsolenoidal flow field. These effects include 1) a retardation of growth of correlation between the magnetic field and the velocity field, 2) the emergence of compressible small scale structure such as massive jets and 3) bifurcation of eddies in the compressible flow field. Differences between the incompressible and compressible results tend to increase with increasing initial average Mach number.

PACS numbers: 52.65.+z, 52.55.Dy, 47.65.+a, 95.30.Qd

## CONTENTS

I.	INTRODUCTION .....	1
II.	NUMERICAL SIMULATIONS .....	5
	A. Formulation .....	5
	B. Initial Conditions .....	8
	C. Numerical Algorithm .....	10
	D. Incompressible Calculations .....	12
III.	RESULTS AND DISCUSSIONS .....	13
	A. Measures of Compressible and Incompressible Phenomena .....	14
	B. Dynamic Alignment and Selective Decay .....	16
	C. Morphology of the Velocity and Magnetic Fields .....	18
	D. Reconnection Phenomena .....	21
	E. Spectral Distributions .....	22
IV.	CONCLUSIONS .....	26
	ACKNOWLEDGEMENTS .....	28
	REFERENCES .....	29
	FIGURES .....	33

Accession For	
NTIS	CRA&I <input checked="" type="checkbox"/>
DTIC	TAB <input type="checkbox"/>
Unannounced <input type="checkbox"/>	
Justification _____	
By _____	
Distribution / _____	
Availability Codes	
Dist	Avail and/or Special
A-1	



# NUMERICAL SIMULATION OF THE COMPRESSIBLE ORSZAG-TANG VORTEX

## I. INTRODUCTION

The theoretical and numerical study of turbulence has concentrated until recently on incompressible media. The motivation for this concentration of effort is the comparative simplicity of the incompressible case—the system of governing equations for the incompressible case is of lower order than the compressible system, and an important constraint (solenoidality) links different components of the velocity. In addition, incompressible fluids have ideal invariants which facilitate analysis of the states to which turbulent, dissipative fluids relax (e.g., [1]). Unfortunately many turbulent media, such as nonconducting neutral gases and space plasmas, are compressible, and the relevance of the incompressible results to their behavior is questionable. Marsch and Mangeney [2], for example, recognized this uncertainty regarding the treatment of turbulence in the solar wind and interplanetary medium, and derived a compressible formulation of magnetohydrodynamics (MHD) in terms of Elsässer variables for application to such problems. Our purpose here is to begin the systematic development and study of numerical data to determine the effects of compressibility on MHD turbulence. The data also provides a basis for interpreting theoretical treatments and devising a more complete theory. In this paper we examine a set of initial conditions that are defined analytically for both incompressible and compressible media. By comparing the results of numerical simulations of the compressible case with incompressible simulations, we identify some of the effects which are introduced by compressibility.

To place the present paper in perspective, we note that at least three other major categories of compressible turbulent phenomena have been pursued. The most obvious is the interaction of a sound or shock wave with a turbulent field or vortices (see, for example, papers by Ting [3], Zang *et al.* [4], and Ribner [5]). Here the emphasis is on the amplification of turbulence or the production of sound. Closely related is the direct production of sound by a turbulent field, which was studied in detail by Lighthill [6, 7]. Third is the production of vorticity *via* compressible effects in an initially irrotational flow. This can occur, for example, through the baroclinic source term in the equation for

the evolution of the vorticity, as shown by Picone *et al.* [8 , 9 , 10]. The vorticity can subsequently evolve into turbulence by interaction of resonant harmonics [11].

This paper treats a fourth category, the evolution of an unbounded compressible turbulent field. Here the medium may interact with itself through internally generated acoustic or magnetoacoustic waves. The property of compressibility also leads to alterations in the morphology and description of the medium exclusive of such waves. Thus our concern is with the dynamics of "compressible" turbulence itself, and a complete treatment requires a fully compressible representation of the entire flow field, including the rotational component. To achieve a useful description of compressible MHD turbulence, we use numerical experiments on analogous incompressible and compressible problems. This is different from the first two research areas mentioned above, in which the standard approach has been to treat the turbulent portion of the fluid as incompressible and separable from compressible wave phenomena such as shocks and sound waves. Such a separation of the incompressible and compressible parts of the flow is consistent with linearization of the governing equations (*e.g.*, [12]). Our approach, however, requires the solution of the full set of nonlinear governing partial differential equations because we treat the entire fluid as compressible.

An accurate solution of the nonlinear equations governing a compressible turbulent field includes phenomena associated with acoustic or shock waves, but, in our case, not as external sources of excitation nor as actions of the turbulent field on external regions. Thus, the turbulence can produce acoustic and shock waves which interact with each other and with the turbulent field itself. In addition to altering the turbulent field, these interactions can generate vorticity through the baroclinic source term in the vorticity evolution equation [9]. Such effects are thus important to our investigations but are not the whole story, as confirmed by the differences between incompressible solutions and homentropic, polytropic compressible solutions for a steady state vortex in an unbounded medium [13]. These differences exist even though the velocity field for the steady state vortex is solenoidal in both cases.

This paper deals with initially average subsonic flows in two-dimensional compressible

magnetofluids in the average Mach number regime from 0.2-0.6 (The limitation to Mach numbers of about 0.6 or less is due to the way in which we specify the fluctuating pressure, as described below). For the magnetofluid there are also compressible alterations to the magnetic source terms in the vorticity equation, which indicate the possibility of vorticity production by the interaction of magnetoacoustic waves and MHD shock waves with the turbulent field. As in the incompressible case, the magnetic field is still constrained to be solenoidal. Note, however, that the absence of the velocity field solenoidality constraint also leads to the presence of a compression term in the magnetic induction equation. This variation in mode coupling between the velocity field and magnetic field implies that the magnetic field can evolve differently in the compressible medium; for example, magnetic flux can accumulate in compression regions.

A noteworthy initial approach to the theory of compressible MHD turbulence by Montgomery *et al.*[14] expresses the fluctuating density as a function of the pressure derived through the usual incompressible formulation. This assumes that incompressible flow is a well defined limit of compressible flow and seeks to determine the spectral index of density fluctuations for "nearly incompressible" MHD turbulence. Shebalin and Montgomery have investigated this model numerically [15]. As mentioned above, Marsch and Mangeney [2] have developed a theoretical framework which extends methods used in the incompressible MHD regime. For the hydrodynamic case, Moiseev *et al.*[16] have used similarity and renormalization group arguments to estimate the deviations of subsonic compressible turbulence from the Kolmogorov spectrum in a noncharged system driven by a Gaussian external force.

Recent computational studies of fully compressible turbulence for noncharged fluids by Passot and Pouquet [17] and Erlebacher *et al.*[18] and for MHD by Dahlburg *et al.*[19] have used random initial conditions with a range of spatial scales. All of these calculations used spectral methods for their accuracy and cost-effectiveness in studying turbulent flows. Earlier studies of compressible MHD turbulence employed finite difference algorithms and initial conditions consisting of at most a few modes [20, 21, 22].

None of the above MHD studies directly compared compressible and incompressible simulations. Erlebacher *et al.* (1987) have compared compressible and incompressible time histories of various statistical quantities in hydrodynamic turbulence [18]. Passot and Pouquet separated the solenoidal and nonsolenoidal components of the velocity and specific kinetic energy fields in order to accomplish this comparison for a dissipative fluid obeying the Navier-Stokes equations for a perfect gas. As indicated above, however, solenoidality of the velocity field is not a sufficient condition for incompressibility of the medium, so that their method does not rigorously separate compressible and incompressible phenomena. In this paper, therefore, we take a somewhat different approach, *viz.*, we compare the evolution of compressible and incompressible magnetofluids starting from the same initial conditions. We perform simulations at several subsonic initial average Mach numbers to determine the effects of increasing compressibility. We use the nonrandom, periodic initial conditions of Orszag and Tang [23]. The initial velocity and magnetic fields each contain only one mode, although not the same one. The level of compressibility is determined by the initial mean thermal pressure magnitude. The model contains an incompressible analog that is well known (*e.g.*, [23], [24], [25], [26], [27] [28]), providing an excellent baseline case for the study of compressible MHD turbulence. These initial conditions thus permit a more direct (less statistical) quantitative and structural comparison of turbulent evolution within compressible and incompressible media and contains most of the significant features of MHD turbulence, including dissipation of magnetic and kinetic energy, reconnection, formation of high density jets, selective decay, dynamic alignment, and the emergence and manifestations of small scale structure (*e.g.*, [29], [30], [31], [32], [33]). A preliminary version of this work has appeared elsewhere [34].

The paper begins with a formulation of the problem, followed by a section describing our numerical methods. Because relatively few numerical treatments of compressible MHD turbulence have been performed, the optimum numerical method and the appropriate equations to integrate are issues in themselves. In the course of our discussion, we review formulations and algorithms that are reasonable candidates for consideration and have



been employed for similar purposes or physical regimes. Section III presents our numerical results, including the significant differences between the compressible and incompressible analogs, for a number of turbulent MHD phenomena. Section IV presents our conclusions and a description of related work in progress.

## II. NUMERICAL SIMULATIONS

### A. Formulation

We start with the nonlinear partial differential equations which govern the behavior of a two-dimensional, compressible, dissipative magnetofluid, written here in a dimensionless form:

$$\frac{\partial \rho}{\partial t} = -\nabla \cdot (\rho \mathbf{v}) , \quad (1a)$$

$$\frac{\partial (\rho \mathbf{v})}{\partial t} = -\nabla \cdot \left[ \rho \mathbf{v} \mathbf{v} - \mathbf{B} \mathbf{B} + \frac{1}{2}(p + |\mathbf{B}|^2) \mathbf{I} - \frac{1}{S_v} \boldsymbol{\tau} \right] , \quad (1b)$$

$$\frac{\partial \mathbf{B}}{\partial t} = \nabla \times \left[ \mathbf{v} \times \mathbf{B} - \frac{1}{S_r} \nabla \times \mathbf{B} \right] , \quad (1c)$$

$$\begin{aligned} \frac{\partial E}{\partial t} = & -\nabla \cdot \left[ (E + p) \mathbf{v} + (|\mathbf{B}|^2 \mathbf{I} - 2\mathbf{B} \mathbf{B}) \cdot \mathbf{v} \right. \\ & \left. - \frac{2}{S_v} \mathbf{v} \cdot \boldsymbol{\tau} + \frac{2}{S_r} (\mathbf{B} \cdot \nabla \mathbf{B} - \nabla \mathbf{B} \cdot \mathbf{B}) \right. \\ & \left. - \frac{\gamma}{\gamma - 1} \frac{1}{S_v Pr} \nabla T \right] , \end{aligned} \quad (1d)$$

$$\nabla \cdot \mathbf{B} = 0 , \quad (1e)$$

supplemented by an equation of state,

$$p = (\gamma - 1)U . \quad (2)$$

The notation in Eqs.(1) and (2) is as follows:  $\rho$  is the mass density,  $\mathbf{v} \equiv (v_x, v_y, 0)$  is the flow velocity,  $p$  is the mechanical pressure,  $\mathbf{I}$  is the unit dyad,  $\mathbf{B} \equiv (B_x, B_y, 0)$  is the magnetic induction field,  $U$  is the internal energy density,  $E$  is the total energy density, given in dimensionless units by

$$E(\mathbf{x}, t) \equiv \rho|\mathbf{v}|^2 + |\mathbf{B}|^2 + U, \quad (3)$$

$T \equiv p/\rho$  is the dimensionless temperature,  $\tau \equiv [(\partial_j v_i + \partial_i v_j) - \frac{2}{3} \nabla \cdot \mathbf{v} \delta_{ij}] \hat{\mathbf{e}}_i \hat{\mathbf{e}}_j$  is the viscous stress tensor, and  $\gamma \equiv 5/3$  is the ratio of specific heats. The thermal conductivity ( $\kappa$ ), magnetic resistivity ( $\eta$ ), and viscosity ( $\mu$ ) are constant and uniform, and we assume that the Stokes relation holds, so that the bulk viscosity is zero [35]. The important dimensionless numbers are the viscous Lundquist number  $S_v \equiv \rho_0 V_A L_0 / \mu$  [36], the resistive Lundquist number  $S_r = V_A L_0 / \eta$ , the Prandtl number  $Pr = c_p \mu / \kappa$ , and the Alfvén number  $A = (V_A^2 / V_0^2)^{1/2}$ . In these definitions,  $\rho_0$  is a characteristic density,  $V_A$  is the Alfvén speed,  $L_0$  is a characteristic length equal to the reciprocal of the minimum wavenumber  $k_{min} = 2\pi/L$  ( $L$  = system length),  $c_p$  is the specific heat at constant pressure, and  $V_0$  is a characteristic flow speed. The thermodynamic normalization sets

$$E_0 = p_0 = B_0^2 / 8\pi = \rho_0 V_A^2 / 2. \quad (4)$$

The characteristic speed of sound is then  $C_{S0}^2 = \gamma p_0 / \rho_0$ . Time ( $t$ ) is measured in units of the Alfvén transit time  $L_0 / V_A$ . For the runs reported here, we set  $S_v = S_r = 50, 100, \text{ or } 200$  and  $Pr = A = 1$ . All of our numerical simulations assume unit magnetic Prandtl number, i.e.,  $\mu / (\rho_0 \eta) = 1$ , so we subsequently consider only the parameter  $S = S_v = S_r$ .

The reader should note that formulations of the numerical problem other than Eqs. (1) are presently being used to study compressible MHD phenomena. Schnack *et al.* [37] use only equations (1b), (1c) and (1e) with the assumption of constant mass density and zero mechanical pressure to model the Reversed-Field Pinch for magnetic fusion. This is a zero- $\beta$  approximation to a very low  $\beta$  plasma, where  $\beta$  is the ratio of the mechanical pressure

to the magnetic pressure. Mikić *et al.*[38] also have used this approximation to model the solar corona (but note that they replace the Eqs. (1c) and (1e) with a magnetic vector potential equation). In addition, they assume that the convection term in the equation of motion is negligible. The applicability of a zero- $\beta$  model in these two cases is debatable. More importantly, mass density fluctuations and gradients in mechanical pressure can play as great a role in MHD turbulence as they do in nonmagnetized fluids.

More common in treatments of compressible flows is the assumption of a homentropic, polytropic medium [22], [39] which satisfies the equation

$$p = Q \rho^\gamma, \quad Q = \text{constant} . \quad (5)$$

This is often called the "polytropic equation of state." Technically speaking, however, a polytropic fluid need not have constant entropy, or equivalently,  $Q$  need not be constant.

Assuming that the fluid is homentropic, Eq. (5) replaces Eq. (1d) for conservation of total energy, and the system to be integrated is then Eqs.(1a)-(1c) and (1e). Note that constant entropy implies that the dissipative terms are zero. Unfortunately, such systems of hyperbolic equations will likely develop magnetoacoustic waves and discontinuities (shocks) in a finite amount of time when the flow is unsteady. The fact that the entropy is constant and uniform throughout the fluid means that the shock solutions of this reduced system of equations cannot satisfy the Rankine-Hugoniot jump conditions, except for very weak shocks [39]. Equation (5) also precludes the generation of vorticity through the baroclinic term ( $\frac{1}{\rho^2} \nabla \rho \times \nabla p$ ) in the vorticity evolution equation [9]. Thus the assumption of a homentropic, polytropic medium cannot account for several important factors in the formation and evolution of compressible MHD turbulence. Our formulation (Eqs.(1) and (2)) provides for all of these effects and for strict conservation of mass, momentum, and energy.

The use of Eq.(5) instead of Eq.(1d) also has important consequences for numerical modeling. In an ideal fluid, the development of discontinuities will result in unstable numerical solutions if a high order explicit integration scheme is used. The computer model

will therefore “blow up.” The addition of sufficiently large dissipative terms, either physical or numerical (*e.g.*, a viscous term in the equation of motion), can result in smooth mathematical and numerical solutions with steep finite gradients instead of shock-like discontinuities [19]. When Eq. (5) is used, such terms are inconsistent with a constant entropy, as mentioned above. In addition, if this “reduced” system of equations is dissipative, then total energy is not conserved, similar to the case of incompressible flow. The shocks would be nonphysical since the Rankine-Hugoniot conditions cannot be satisfied. The size of the coefficient of viscosity that is necessary to guarantee numerical stability for an explicit algorithm varies with the situation. A fully implicit or semi-implicit integration scheme can ensure that finite acoustic or magnetoacoustic waves are filtered out of the solution [18, 41]. This should provide a stable solution, although such models cannot represent the effects of finite amplitude waves in a turbulent compressible fluid.

## B. Initial Conditions

For initial conditions we use the vortex system of Orszag and Tang (1979):

$$\rho(x, y, t = 0) = 1, \quad (6a)$$

$$\mathbf{v}(x, y, t = 0) = -\sin y \hat{\mathbf{e}}_x + \sin x \hat{\mathbf{e}}_y, \quad (6b)$$

and

$$\mathbf{B}(x, y, t = 0) = -\sin y \hat{\mathbf{e}}_x + \sin 2x \hat{\mathbf{e}}_y, \quad (6c)$$

where  $\hat{\mathbf{e}}_x$  and  $\hat{\mathbf{e}}_y$  are unit vectors in the  $x$  and  $y$  directions respectively. The initial mechanical pressure,  $p(t = 0)$ , is decomposed into a mean part,  $\langle p(t = 0) \rangle$ , and a fluctuating part,  $p_f(t = 0)$ . We set  $p_f(t = 0)$  equal to the appropriate incompressible pressure distribution, which is obtained by applying a divergence operator to the incompressible MHD equation of motion (Eq. (1b') below) and then inverting the resulting Poisson equation.

This specification of  $p_f(t=0)$  puts a physical lower limit on  $\langle p(t=0) \rangle$ , *i.e.*, we must select  $\langle p(t=0) \rangle$  such that  $p(x, y, t=0) = \langle p(x, y, t=0) \rangle + p_f(x, y, t=0) > 0$  everywhere in the system. Figure 1 shows the initial form of the flow field in the form of streamline plots of the velocity and magnetic field.

Notice that, for a polytropic, homentropic, compressible fluid (Eq.(5)), our initial conditions of a spatially varying mechanical pressure and a spatially constant mass density would contradict Eq.(5). However, in our formulation, the temperature varies spatially with the mechanical pressure, so that the mass density can in fact be constant. Because of this, any steady state solenoidal velocity field that can exist in an incompressible medium has a direct analog in a compressible medium. An alternative to our initial conditions would be to use Eq. (5) to get an approximately consistent mass density field rather than Eq. (1a); however, the mapping onto the initial conditions of the incompressible solution would then be altered. We have also used a flat initial pressure profile along with Eqs. (6a)-(6c) and have found that the early behavior ( $t \leq 1.0$ ) is somewhat different in that, *e.g.*, growth of correlation is more rapid. This is caused by the small expansion of the vortices necessary to set up a pressure gradient in response to the centrifugal forces that are present. In the calculations of Dahlburg *et al.*[19], the pressure and mass density were flat and broadband noise was used to construct the magnetic field. The initial velocity field resulted from rotating the magnetic field through a fixed angle consistent with the desired value of the initial correlation  $\xi$ . Dahlburg *et al.* found that again the evolution of global integrals was smooth after an initial rapid jump in correlation.

Returning to the definition of initial conditions, the normalization in Eq. (4) gives the local Mach number  $\mathcal{M}$  as

$$\mathcal{M}^2 = \frac{2\rho|\mathbf{v}|^2}{\gamma p} . \quad (7a)$$

To obtain a "characteristic" Mach number  $M$  at time  $t=0$  for the flows in our calculations, we substitute  $\rho = \langle \rho(t=0) \rangle$ ,  $p = \langle p(t=0) \rangle$ , and  $|\mathbf{v}| = \sqrt{\langle \mathbf{v}^2(t=0) \rangle}$  into Eq. (7a). We

then choose initial values of  $\langle p \rangle$  to give  $M = 0.2, 0.4$ , or  $0.6$ . The lower limit on  $\langle p \rangle$ , described earlier, implies an upper limit on the values of  $M$  that we can obtain, which for our initial conditions is about  $0.6$ . Figure 1 shows the initial form of the pressure field and local Mach number,  $\mathcal{M}$ , for the  $M = 0.6$  case. It can be seen that  $\mathcal{M}$  varies widely over the system. Note that, because of the relative magnitudes of the parameters in Eqs. (6),  $\langle \beta \rangle$  decreases as  $M$  increases in our simulations according to

$$\beta \equiv \frac{p}{|\mathbf{B}|^2} = \frac{2\rho|\mathbf{v}|^2}{\gamma\mathcal{M}^2|\mathbf{B}|^2} \quad (7b)$$

By again substituting average initial values for the various parameters, one obtains characteristic  $\langle \beta \rangle$  values of  $30.0, 7.5$ , and  $3.3$ , respectively.

### C. Numerical Algorithm

In computations of two dimensional MHD systems, it is more economical to replace the magnetic induction equation (Eq. (1c)) by the simpler magnetic vector potential equation,

$$\frac{\partial a}{\partial t} = \mathbf{v} \times \mathbf{B} + \frac{1}{S_r} \nabla^2 a, \quad (1c')$$

where  $a$  is the  $z$ -component of the magnetic vector potential, and  $\mathbf{B} = \nabla \times a \hat{\mathbf{e}}_z$ . The solenoidality of the magnetic field (Eq. (1e)) is then trivially ensured since  $\nabla \cdot \mathbf{B} = \nabla \cdot \nabla \times a \hat{\mathbf{e}}_z = 0$ . To solve the governing equations (1a, 1b, 1c', and 1d) our code, *CRUNCH2D*, implements a Fourier collocation method [42]. The algorithm employs an isotropic truncation in Fourier space at each time-level [18], i.e., all modes with  $|\mathbf{k}| > \frac{N}{2}$  are set equal to zero, where  $\mathbf{k}$  is the Fourier wavevector and  $N$  is the number of (one dimensional) Fourier modes. The modified Euler method, a second-order Runge-Kutta scheme [43], discretizes time. The time step,  $\Delta t$ , is limited by a compressible MHD Courant-Friedrichs-Lewy (CFL) number,

$$N_{CFL} = \sup \left\{ \frac{(|\mathbf{v}| + C_S + V_A)\Delta t}{h} \right\} \leq 0.3, \quad (8)$$

where  $C_S$  = sound speed, and  $h = 2\pi/N = \Delta x = \Delta y$ . Our simulations consume approximately  $18 \mu s$  per time step per grid point on the NRL CRAY X-MP/24. For Lundquist

numbers of 50, 100, and 200, we use, respectively,  $64^2$ ,  $128^2$ , and  $256^2$  collocation points. The calculations with  $64^2$  collocation points require approximately 0.12 million words of core memory.

The contrast between the above spectral techniques for modeling compressible flow and finite difference algorithms, which have been in wider use for compressible MHD flows [20, 21, 22], deserves some comment. Finite difference algorithms permit implementation of complex boundary conditions which are presently more difficult or impossible for spectral methods. In addition, finite difference shock-capturing schemes are able to maintain steeper and narrower shocks than their spectral counterparts. Given that the time-scales of interest in the modeling of turbulence are much longer than shock transit times and given that we are presently studying initially average subsonic flows, this difference is less important than others.

On the other hand, finite difference approximations to first and second derivatives introduce significant noise into source terms, reducing the accuracy of the solution. Solving the magnetic induction equation (Eq. (1c)) instead of that for the vector potential (Eq. (1c')), will ensure that only one derivative is necessary to compute the current density, at the additional expense required to time-advance two dependent variables instead of one. A careful formulation of the finite difference equations and the differencing grid are then necessary to maintain a solenoidal magnetic field [44]. The Fourier collocation technique permits the modeling of a much broader range of spatial scales than do finite difference techniques of comparable cost. This is a major advantage for studies of both compressible and incompressible turbulence [42]. Finally, spectral methods have become the method of choice for general studies of incompressible turbulence in systems with simple boundary conditions [42], and the ability to use similar algorithms for our compressible and incompressible calculations reduces the influence of numerical factors in comparing them.

A final point regards the use of the conservation form of the model Eqs. (1). The mechanical pressure is then a "derived" quantity, computed as the difference of the total

energy density and the sum of the kinetic and magnetic energy densities, as indicated by Eqs. (2) and (3). Now consider as examples (a) low  $\beta$  regions in plasmas, in which the mechanical pressure is, by definition, much smaller than the magnetic pressure, and (b) local regions near shocks, where the kinetic energy can be much larger than the internal energy. In explicit schemes, each differential equation in the set, Eqs. (1), is solved separately from the others, using parameter values from the previous time step. If the resulting solutions for the field variables are not "synchronized" in phase, errors in the mechanical pressure can be as large as the mechanical pressure itself. We have seen this in finite difference calculations, and spectral methods could theoretically have the same problem. This has driven some modelers to use a pressure equation instead of Eq. (1d) for conservation of total energy, requiring monitoring of the latter [45]. A "fix" for this problem in modeling shocks is the use of sufficient physical diffusion near the shocks. At the Lundquist and Mach numbers used here, the physical diffusion has been sufficient to ensure well-behaved solutions for the mechanical pressure.

#### D. Incompressible Calculations

To help identify the turbulent effects which are due to compressibility, we run incompressible calculations with a second simulation code. In this limit the mass density remains constant and uniform, and total energy is not conserved in the presence of finite dissipation. The form of the incompressible equations solved by this second code is:

$$\frac{\partial \mathbf{v}}{\partial t} = \mathbf{v} \times \omega \hat{\mathbf{e}}_z - \nabla \Pi + j \hat{\mathbf{e}}_z \times \mathbf{B} + \frac{1}{S_v} \nabla^2 \mathbf{v} , \quad (1b')$$

coupled with the velocity field solenoidality constraint:

$$\nabla \cdot \mathbf{v} = 0 \quad (1a')$$

and Eq. (1c'). The pressure head,  $\Pi$ , is given by  $p + 0.5 * |\mathbf{v}|^2$ . The integration of these equations is accomplished with a two-dimensional version of the *MHDBOX* explicit Fourier collocation algorithm employed by Dahlburg *et al.*[46] for studying the turbulent decay of



force-free magnetic fields. The temporal integration is again modified Euler. The algorithm also employs an isotropic truncation in Fourier space. We use the same initial conditions, eqs. (6), with appropriate adjustments to account for the different normalization.

### III. RESULTS AND DISCUSSION

Our investigation of compressibility in the Orszag-Tang vortex model relies primarily on time-dependent area integrals, contour diagrams, generalized streamline plots, and wavenumber spectra. The temporal evolution of area integrals permits a direct comparison of global compressible effects with their incompressible counterparts and can also show the effects of dissipation, as parameterized by the Lundquist numbers. The bracket notation represents a volume average, *i.e.*, an average of some function ( $f$ ) over the entire grid ( $\mathcal{G}$ ),

$$\langle f \rangle = \frac{\int_{\mathcal{G}} f(x, y, t) dx dy}{\int_{\mathcal{G}} dx dy} , \quad (9)$$

and thus applies to global features of the flow. We use contour plots and generalized streamline plots to show how compressibility affects the local structures of the flow field and magnetic field and to reinforce inferences from the global integrals. The streamline plots indicate direction of a vector function at a given point, but not the magnitude of the function. Streamline plots are the best way to visualize the form of the compressible flow field. Since we often compare the form of the velocity field with that of the magnetic field, we also represent the magnetic field this way, rather than using plots of magnetic vector potential contours. The wavenumber spectra indicate interactions between, and the importance of, fluctuations at various scale lengths in the magnetofluid. Since the spreading out of fluctuations in Fourier space depends on the form of the nonlinearities in the governing equations, we expect that compressibility will affect the form of the observed spectra.

## A. Measures of Compressible and Incompressible Phenomena

Some initial observations about the global integrals are necessary. First assume that the appropriate boundary conditions exist for surface integrals to vanish. Because of the variations in mass density and the dependence of the thermal pressure on temperature and mass density, some quantities which are constants of the motion in nondissipative, incompressible, MHD turbulence are no longer constants of the motion in the corresponding compressible flows. In two dimensions, these quantities are  $\langle \mathbf{v} \cdot \mathbf{v} + \mathbf{B} \cdot \mathbf{B} \rangle$ , proportional to total energy in an incompressible MHD system ( $E_i$ ), the mean square magnetic vector potential  $\langle a^2 \rangle$ , and the cross helicity,  $H_c \equiv \langle \mathbf{v} \cdot \mathbf{B} \rangle$ . Corresponding conserved functions for compressible media exist for the first two quantities: total energy, given by Eq.(3), and the material integral  $\langle \rho a^2 \rangle$  [47]. Figure 2 shows data on  $\langle \rho a^2 \rangle$  and  $\langle a^2 \rangle$  for a typical dissipative compressible calculation. Notice that  $\langle a^2 \rangle$  fluctuates about a decreasing monotonic line given by  $\langle \rho a^2 \rangle$ . The smooth decrease of the latter is characteristic of quantities that are constant in an ideal fluid. The reason for the proximity of the two functions is the initial condition  $\rho = 1$ . In general, the normalized ratio of inviscid constants,  $\langle \rho a^2 \rangle / \langle \rho \rangle$ , is best for such comparisons.

For some boundary conditions (e.g., doubly periodic), Horiuchi and Sato [21] have shown that  $H_c$  should be an ideal constant of the motion when the mass density is uniform and constant (incompressible fluid) or for a homentropic, polytropic fluid. Our assumption of constant  $\gamma$  is equivalent to the assumption that the fluid is polytropic (but not homentropic). In an ideal compressible fluid, the only sources of dissipation are shock discontinuities or finite sound waves, which will steepen into shocks [48]. Since the intensity of such waves is smaller for lower Mach number, the fluid should have a more spatially uniform entropy as Mach number decreases, and deviations of the pressure from the homentropic, polytropic equation of state, Eq.(5), also should be small. These arguments and the theoretical arguments of Horiuchi and Sato, when applied to the more general class of compressible media in our calculations, lead us to expect the following conditions to hold:

- (1) The plots of incompressible and compressible values of  $H_c$  versus time should become

more similar as Mach number decreases and;

(2) The spatial variation of the polytropic coefficient,  $p/\rho^\gamma$ , should decrease as Mach number decreases.

The first statement indicates that  $H_c$  behaves more as an approximate ideal invariant as Mach number decreases, since we know that it is invariant in the incompressible case. Unfortunately our results could not rule out the possibility that  $H_c$  was also invariant at the higher Mach numbers. The second statement indicates that, as Mach number decreases, the fluid approaches the homentropic, polytropic case, for which  $H_c$  should be invariant. The theory of Horiuchi and Sato implies that, at higher values of  $M$ , on the other hand,  $H_c$  should no longer be an approximate ideal invariant of the system. Further, the arguments of Horiuchi and Sato, along with our results, would imply that the reason was related to the dissipative effects of compressible waves and the accompanying spatial variation of entropy, even in an ideal compressible fluid [48]. Both conditions (1) and (2) hold for our calculations. Figure 3 shows that the evolution of cross helicity for a Mach number of 0.2 is nearly identical to that in the incompressible case. The plot for  $M = 0.6$  differs considerably, indicating that  $H_c$  no longer behaves as the ideal, incompressible invariant does. From this plot, of course, we cannot state with certainty that  $H_c$  is no longer an approximate ideal invariant of the compressible system when  $M$  is 0.4 or greater.

Figure 4 shows contours of the polytropic coefficient for  $S = 100$  and  $M = 0.2$  and 0.6 at early and late times ( $t = 2$  and  $t = 8$ ). This gives us a picture of the spatially varying entropy as well. For the  $M = 0.2$  case, the ratio of maximum and minimum values of the polytropic coefficient is 1.27 at  $t = 2$ , and 1.12 at  $t = 8$ . For the  $M = 0.6$  case, the ratio of maximum and minimum values of the polytropic coefficient is about 8.90 at  $t = 2$ , and 2.78 at  $t = 8$ . The ratio is more nearly one at lower  $M$ , and thus the entropy is more uniform, showing the approach to Eq. (5) with decreasing Mach number. The decline of this ratio with time for both Mach number cases indicates that the amplitudes of finite magnetoacoustic waves are decreasing with time as  $\mathbf{v}$  becomes more aligned with  $\mathbf{B}$  and as the mass density becomes more uniform. Apparently the system is approaching

a quasisteady state which is also approximately homentropic.

## B. Dynamic Alignment and Selective Decay

Dynamic alignment is representative of a more general class of turbulent fluid behavior known as self-organization. Hasegawa [49] has reviewed the extensive work on the incompressible MHD case. Only recently have studies of the compressible MHD case taken place, using finite difference algorithms [20, 21, 22] or spectral techniques [19, 34]. The measure of correlation often used in incompressible calculations is the ratio of the cross helicity ( $H_c$ ) to incompressible total energy ( $E_i$ ), given by:

$$\xi = \frac{H_c}{E_i} = \frac{2\langle \mathbf{v} \cdot \mathbf{B} \rangle}{\langle |\mathbf{v}|^2 \rangle + \langle |\mathbf{B}|^2 \rangle} \quad (10)$$

This correlation coefficient relates the dynamic alignment process to selective decay for the incompressible case (*cf.* [50], [26], [51]). In the compressible case, the numerator and denominator which define  $\xi$  are no longer rugged invariants, although analogous quantities may be defined. An alternative measure, which is perhaps more meaningful for the compressible case, is the alignment factor:

$$\alpha = \frac{\langle \mathbf{v} \cdot \mathbf{B} \rangle}{\sqrt{\langle |\mathbf{v}|^2 \rangle \langle |\mathbf{B}|^2 \rangle}} \quad (11)$$

This is somewhat closer to the conventional definition of a normalized correlation.

Figure 5 shows  $\xi$  and  $\alpha$  for the incompressible case and as a function of  $M$  with Lundquist number  $S = 100$ . We see that, for both the incompressible and compressible cases,  $\mathbf{v}$  and  $\mathbf{B}$  become more correlated as a function of time and that the growth of correlation for  $M = 0.2$  is nearly identical to that of the incompressible system. As  $M$  increases, however, the correlation at any given time up to  $t = 10$  is less. Some variation from this is seen in the evolution of  $\alpha$ . By both measures, though, compressibility retards the dynamic alignment process in the Orszag-Tang vortex. The variation with  $S$  (not shown) is qualitatively similar to that found for incompressible calculations [51]. As  $S$  increases, the correlation at any given time is less. Finally, note that  $\alpha$  evolves in a more

erratic manner than  $\xi$ , but that both  $\alpha$  and  $\xi$  exhibit the same secular trend, *viz.*, an increase with time.

Past treatments of this phenomenon have attributed the temporal increase in alignment in incompressible media to selective decay of the energy,  $E_i$  ( $(\langle |\mathbf{v}|^2 \rangle + \langle |\mathbf{B}|^2 \rangle)/2$ ), relative to the cross helicity,  $H_c$  ( $\langle \mathbf{v} \cdot \mathbf{B} \rangle$ ) ([50], [26], [51]). Similar arguments apply to the compressible case as well. Figure 3 shows, however, that the functional dependence of selective decay on  $M$  is different from the dependence on  $S$ . First consider variation with  $S$  for constant  $M$  and at a particular time  $t$ . Figures 3c and 3d show that both  $H_c$  and  $E_i$  increase with increasing  $S$ . However, the increase in  $E_i$  is greater, thus causing a reduction in  $\alpha$  and  $\xi$  as  $S$  increases. This is also the case for incompressible media [26].

Now consider variations in Mach number in Figs. 3a and 3b. As  $M$  increases with constant  $S$ ,  $H_c$  decreases. The quantity  $E_i$ , however, varies little with  $M$ . Figure 5 shows that the magnetic and kinetic energy components, taken separately, also vary weakly with  $M$ . Because  $\rho$  is  $O(1)$ , and  $\langle |\mathbf{v}|^2 \rangle \sim \langle |\mathbf{B}|^2 \rangle$ , the denominators of the alignment measures, Eqs. (10) and (11), will also show little variation with Mach number. Thus the reduction in alignment with increasing  $M$  is primarily due to a corresponding reduction in  $H_c$ . The discussion below of morphology of the compressible flow reveals at least one effect which could cause this. As shown in the next subsection, the velocity field exhibits the emergence of increased small scale structure and greater structural variation with increasing  $M$  while the magnetic field, in relative terms, does not. This results in more local reductions in alignment between  $\mathbf{v}$  and  $\mathbf{B}$  at a given time, as  $M$  increases.

We also observe that the dilatation,  $\mathcal{D} \equiv \nabla \cdot \mathbf{v}$ , is generally nonzero in the compressible fluid and increases in magnitude with  $M$ . Since viscous dissipation includes contributions from a term dependent on the gradient of  $\mathcal{D}$ , the overall dissipation of the velocity field can increase with the amplitude of compressible effects. This term is important, for example, in the damping of acoustic and shock waves. Such dissipation could lead to reductions in  $\langle |\mathbf{v}|^2 \rangle$  and  $H_c$  with increasing  $M$ . For the total kinetic energy to remain approximately the same as  $M$  changes (Fig. 5), the change in the local mass density must compensate

for the local changes in  $v$ .

### C. Morphology of the Velocity and Magnetic Fields

The generalized streamline plots and the contour plots presented in this section provide a detailed visualization of the velocity and magnetic fields as the Orszag-Tang vortex evolves in a compressible medium. Again the incompressible solution provides a baseline for interpreting the results for a compressible medium. Figure 6 shows the incompressible velocity field and the corresponding compressible velocity fields at  $t = 2$  as for  $M = 0.2, 0.4$ , and  $0.6$  with  $S = 100$ . Notice that the  $M = 0.2$  compressible solution closely resembles the incompressible solution in Fig. 6, confirming the impression obtained from the plots of global averages that low Mach number MHD closely resembles incompressible MHD. These two cases resemble each other for all the other times plotted (not shown). Also apparent in the compressible calculations is the shear flow corresponding to two high density jet structures emanating approximately horizontally from the center of the system, at which reconnection is occurring. At  $M = 0.6$ , the large vortex structures in the middle of the system differ considerably in shape and smoothness from those present at the lower Mach numbers and in the incompressible case. We attribute this to differences in the rates of reconnection occurring at the center and edges of the system for the various calculations (next section). The reconnection and the velocity shear at the center of the system are most striking in Fig. 6 at the highest Mach number ( $M = 0.6$ ). Figure 6 also shows the magnetic field for the incompressible and  $M = 0.6$  cases at the same time ( $t = 2$ ). This field appears slightly less rounded as the Mach number increases, but overall the magnetic field structure changes much less than the velocity field with increasing Mach number.

Figure 7 compares the incompressible and  $M = 0.2, 0.4$ , and  $0.6$  solutions for  $S = 100$  at time  $t = 4$ , and provides evidence of splitting of vortices at the higher Mach numbers. At lower Mach numbers and in the incompressible medium, a large vortex pair resides in the middle. At  $M = 0.6$ , each vortex has apparently split into two separate, smaller vortices with an X-point in between. The cause of this splitting with increased Mach number apparently is the accompanying nonlinear increase in the amplitude and steepness

of fluctuations in the fluid variables, which can cause appreciable sources of vorticity at smaller scales [9]. If  $S$  is held constant while  $M$  increases, the effects of viscous dissipation decrease relative to compressible sources of vorticity.

We digress to consider compressible vorticity generation in greater detail. In a two-dimensional compressible magnetofluid, the vorticity equation is:

$$\begin{aligned}\frac{\partial \omega}{\partial t} &= -\mathbf{v} \cdot \nabla \omega - \omega \nabla \cdot \mathbf{v} + \frac{1}{2} \frac{\nabla \rho \times \nabla p}{\rho^2} + \mathbf{B} \cdot \nabla \frac{j}{\rho} + \frac{1}{S_v} \nabla^2 \omega \\ &= -\nabla \cdot (\mathbf{v} \omega - \frac{\mathbf{B} j}{\rho}) + \frac{1}{2} \frac{\nabla \rho \times \nabla p}{\rho^2} + \frac{1}{S_v} \nabla^2 \omega\end{aligned}\tag{12}$$

In a two-dimensional incompressible magnetofluid, the vorticity equation simplifies to:

$$\frac{\partial \omega}{\partial t} = -\mathbf{v} \cdot \nabla \omega + \mathbf{B} \cdot \nabla j + \frac{1}{S_v} \nabla^2 \omega .\tag{13}$$

Unlike incompressible MHD, the vorticity quadrupole production term for compressible flow also depends on the mass density convected into the reconnection region (*cf.* [52]). This dependence will tend to enhance the quadrupole over the incompressible result in regions of rarefaction (we note parenthetically that this term  $\mathbf{B}j/\rho$  also is significant for dilatation production, *i.e.*,  $\partial \mathcal{D}/\partial t \propto \nabla \times \mathbf{B}j/\rho$ ). The baroclinic term will generate vorticity in any regions where gradients in the mass density and the pressure are not aligned. The most prevalent baroclinic source of vorticity is an asymmetric pressure distribution, such as that which arises at the current sheet produced by reconnection in the center of the system, leading to larger amplitude vorticity at the top and bottom of the magnetic islands and vortex bifurcation. Such pressure distributions produce shocks or finite amplitude waves, which interact with each other and with the accompanying nonuniform mass density distribution to produce or alter local vorticity. The high density jets associated with the reconnection are also a source of significant velocity shear and vorticity.

In addition to vortex splitting, compressibility appears to generate more small scale structure than would otherwise be present. Figure 8 shows this by comparing the  $S = 200$

incompressible and compressible  $M = 0.6$  solutions at time  $t = 8$ . A higher Lundquist number, by itself, leads to more structure. However, the  $M = 0.6$  cases in Figures 7d and 8b show considerable increases in small scale structuring over their incompressible counterparts. Figure 9 shows the velocity field magnitude for  $M = 0.6$  at  $t = 4$ . We see that the regions with the most small scale vortex structure in the streamline plots also have the lowest velocities. Hence differences in the small scale structure among the various cases do not dominate the dynamics.

Figure 10 shows the magnetic field at a later time,  $t = 8$ , as a function of Mach number. Relative to the velocity field, the magnetic field again shows the emergence of much less smaller scale structure as  $M$  increases. Comparison with the velocity field plot at  $t = 8$  (Fig. 7) illustrates the characteristic feature of dynamic alignment, *viz.* the development of a higher degree of alignment between the magnetic field and the velocity field. Since the velocity field shows more significant alteration in structure at higher Mach numbers, the alignment with the magnetic field must be relatively less at any given time. This is a possible explanation for the trend shown by the global integrals in Fig. 5.

Figure 11 shows contours of the dilatation,  $\mathcal{D}$ , for  $M = 0.2$  and  $0.6$  and  $S = 100$  at  $t = 2$ . Positive values of  $\mathcal{D}$  indicate regions of rarefaction, negative values indicate compression. The magnitude of  $\mathcal{D}$  is a measure of the level of compression and rarefaction in the magnetofluid. The dilatation changes markedly as  $M$  increases. The peak positive and negative values,  $\mathcal{D}_{\max}$  and  $|\mathcal{D}_{\min}|$ , are roughly equal at  $M = 0.2$  while  $|\mathcal{D}_{\min}|$  is greater than  $\mathcal{D}_{\max}$  by 13% and 55%, respectively, at  $M = 0.2$  and  $0.4$ . In addition,  $\mathcal{D}_{\max}$  increases by a factor of 5.7 from  $M = 0.2$  to  $0.4$  and by a factor of 4.3 from  $M = 0.4$  to  $0.6$ . Similarly  $|\mathcal{D}_{\min}|$  increases by respective factors of 6.2 and 6.0. These factors do not give an unambiguous Mach number dependence for  $\mathcal{D}_{\max}$  and  $\mathcal{D}_{\min}$ , but they do show that the variation with  $M$  is markedly nonlinear.  $|\mathcal{D}_{\min}|$  is usually greater than  $\mathcal{D}_{\max}$  for  $M = 0.6$  at other times  $t \leq 10$ . For the exceptions, the two are approximately equal. The trend of increases of these parameters with increasing  $M$  holds at all times which we investigated. The difference between  $|\mathcal{D}_{\min}|$  and  $\mathcal{D}_{\max}$  can be as high as a factor of 5. In addition, the



dilatation rate increases for increasing  $S$  and fixed  $M$ . For the  $M = 0.6$  case, as  $S$  is increased from 100 to 200,  $|\mathcal{D}|_{\max}$  increases by a factor of 2.5 (at  $t = 2$ ). This results from the accompanying decrease in dissipation relative to the magnitude of compressible fluctuations, thus reducing dissipative smoothing of the velocity field.

We briefly comment on compressible calculations with varying Lundquist number  $S$ , holding the Mach number fixed. The trends observed for incompressible calculations hold for the compressible calculations, as well. However, for  $M = 0.6$  and  $S = 200$ , the relative amount of small scale structure is higher than in the corresponding incompressible case. This is evident in Fig. 8. Our calculations have not covered sufficiently large Lundquist numbers to determine whether the transition to a fully developed turbulent field occurs earlier for higher values of  $M$ , but the presence of more small scale structure strongly indicates this possibility, possibly intermittently in regions of higher local Mach number. Note that the plots of global integrals indicate that the growth of correlation decreases for either increasing  $S$  or  $M$  with the other held fixed.

#### D. Reconnection Phenomena

Figure 12 shows contour plots of the electric current density and the vorticity at time  $t = 2$  for variable  $M$  and with  $S = 100$ . The current sheet in the center corresponds to the sheared magnetic field occurring there, as in the incompressible Orszag-Tang vortex system [23]. There is some quantitative variation in the electric current density as the Mach number increases, but little qualitative variation. This variation primarily reflects a difference in the “scheduling” of events in the system. In particular, increased compressibility appears to retard the formation of the current sheet centered on the vertical edges of the periodic box. At later times the central current sheets stretch to the point where they exhibit a secondary tearing instability [53]. Because of the interaction between the velocity and magnetic fields at this time, a region of sheared flow coexists with the current sheet. We see the familiar vortex quadrupoles centered on the current sheet ([54], [52]). In addition, isolated high vorticity regions form elsewhere in the box as  $M$  increases, *e.g.*, near the upper left corner of Figure 12d. The magnetic and kinetic enstrophies,  $\langle j^2 \rangle$  and  $\langle \omega^2 \rangle$ ,

are shown in Figures 5e and 5f, respectively, as functions of time for varying  $M$  and  $S = 100$ . These averages show small variation with Mach number and a roughly linear variation with Lundquist number (not shown in the figure). As the Mach number increases the most notable features are a decrease in the peak  $\langle j^2 \rangle$  and the increasing fluctuations in  $\langle \omega^2 \rangle$ .

Resistive heating in the central region, due to the current sheet, produces a massive jet shown in Fig. 13 at  $t = 2$  for variable  $M$ ,  $S = 100$ . As  $M$  increases: (1) the peak density in the jet increases (For the  $M = 0.2$  case peak density in the jet is about 6% above the initial value, while for the  $M = 0.6$  case the peak density is about 110% above the initial value); (2) the gradients in the mass density increase; and (3) the jet becomes more collimated. It is interesting to note that this jet resembles radio wavelength images of astrophysical jets, although we do not speculate that the cause of such objects is the same. Figures 13c and 13d, at a later time ( $t = 8$ ), show that the jet material has spread in the transverse direction and forms a much less distinct structure. The temperature (not shown) contains evidence of both the central vortex and magnetic structures and of the jet.

Also worthy of note is the reconnection occurring across the left and right (periodic) boundaries. This reconnection is apparent from the magnetic field line plots in Figs. 6 and 10 and also from contour plots of current density and vorticity in Fig. 12, which show the presence of current and vortex sheets. We do not see evidence of jets at the boundaries, but the vorticity plots do show the existence of shear flows at the “center” ( $x = \pi, y = \pi$ ) and “edges” ( $(0, y)$  and  $(2\pi, y)$ ) of the computational box. As the Mach number increases in Figs. 12 and 13, the shear at the “edges” becomes weaker relative to that at the “center” of the computational box.

## E. Spectral Distributions

As described above, compressible flow morphology indicates the presence of more small scale structure as the initial average Mach number is increased. This conclusion also

is borne out by a study of the volume averaged spectral distributions of various quantities. Two questions emerge naturally: 1) what are the spectral distributions of compressible quantities, *e.g.*, the mass density, since they have no incompressible analogue, and 2) how does compressibility affect the spectra of quantities with incompressible analogues (*e.g.*, the magnetic energy)? In general, at any given time the spectral distributions show more excitation in the small spatial scales for all of these quantities accompanied by a slight decrease in the slope of the high-wavenumber regions as  $M$  is raised. This implies that the usual caveat about increasing the numerical resolution as the Lundquist (Reynolds-like) number increases also should be extended to the Mach number.

Figure 14 shows spectral plots of the mass density at several different times for the  $M = 0.2$  and  $0.6$  cases. One outstanding feature in these plots is the rapid excitation of the density at small spatial scales, implying that nonsolenoidal flows are well-developed after one Alfvén transit time. Comparison shows that the higher Mach number case is, for any given time, in a more highly excited state (the level of excitation is described roughly by  $\delta\rho/\rho \propto M^2$ ). Spectra for both Mach numbers shown exhibit a rise in excitation, peaking at about  $t = 2$ , followed by a gradual decay.

The conclusion that increasing compressibility leads to more small scale structure is straightforward with respect to a quantity such as the mass density — since the mass density fluctuations are zero by hypothesis in the incompressible case. What about a quantity, like the magnetic field, which fluctuates in both cases? How will it be affected by variations in the Mach number? Figure 15 shows spectral plots of the magnetic energy. Here again we find higher excitation, primarily in the short wavelengths, as the initial average Mach number is increased. The longer wavelengths are not affected as strongly, as might have been expected from the field morphology. Hence the slope of the distribution increases slightly in the high wavenumber range as the Mach number is raised, which suggests that the theory of Moiseev *et al.*[16] might be extended to the MHD case.

We next decompose the velocity field into solenoidal and nonsolenoidal parts, and compare their spectra in Figure 16 at various times for the  $M = 0.6$  case (*cf.*[17]). To

obtain the solenoidal part, we compute

$$\frac{|\mathbf{k} \times \tilde{\mathbf{v}}(\mathbf{k})|^2}{|\mathbf{k}|^2}.$$

where the tilde denotes a Fourier transformed quantity. The nonsolenoidal part is given by

$$\frac{|\mathbf{k} \cdot \tilde{\mathbf{v}}(\mathbf{k})|^2}{|\mathbf{k}|^2}.$$

Our earlier conclusion that compressible excitations develop quickly is borne out by the nonsolenoidal spectra. In the  $M = 0.6$  case, there is almost an equipartition between the two velocity fields, except at the very longest wavelengths. At the later time the nonsolenoidal field is more excited at the smaller scales than the solenoidal field. For the  $M = 0.2$  case (not shown), the solenoidal part of the field generally is more excited than the nonsolenoidal part, especially in the larger scales.

A comparison with the spectral data of Passot and Pouquet (1987) on nonmagnetized fluids initialized with broadband noise can help us to analyze our result of an approximate equipartition between the solenoidal and nonsolenoidal components of the velocity field. We concentrate on the only case which they presented for subsonic flow,  $M = 0.028$ , although this is far below the range which we investigated. In their simulation, the initial velocity field was almost entirely solenoidal. For small initial mass density fluctuations relative to  $M^2$ , Passot and Pouquet found the spectrum to be "quasi-incompressible" at all times. When  $\delta\rho/\rho > M^2$  at  $t = 0$ , the initial, almost entirely incompressible, velocity field changed in two characteristic times to a state in which the nonsolenoidal component comprised over 70% of the kinetic energy.

In our case, the initial density fluctuations are zero. In the absence of the magnetic field, the density would remain constant as the kinetic energy decayed to zero, and the behavior should be quasi-incompressible, as observed by Passot and Pouquet. The dissipation of the magnetic field, however, provides a source of driving energy which can cause an appreciable compressible component. The transient character of this energy source

and the fact that the compressible system is otherwise identical to the incompressible system at very early times and quite similar at later times, indicates that an appreciable incompressible component could be present as well. Under these conditions, approximate equipartition between the solenoidal and nonsolenoidal components seems reasonable. At the lower Mach numbers, one might expect a higher relative level of solenoidality than at the higher Mach numbers.

In Figure 17 we show the normalized cross-helicity,  $\chi$ , defined as:

$$\chi(k) = 2 \frac{\tilde{\mathbf{v}}^*(k) \cdot \tilde{\mathbf{B}}(k)}{|\tilde{\mathbf{v}}(k)|^2 + |\tilde{\mathbf{B}}(k)|^2},$$

for  $M = 0.2$  and  $0.6$  and  $S = 100$  at early, middle, and late times. Incompressible numerical simulations have shown that  $\chi(k)$  tends to bifurcate as time evolves ([50], [26], [51]). Since  $\chi(k) \propto H_c(k)/E_i(k)$ , this indicates that one sign of cross helicity dominates at large spatial scales, while oppositely signed cross helicity dominates at small spatial scales. We note the development of a bifurcated state (i.e., in which  $\chi$  has different signs at the large and small scales) at later times for both Mach numbers. For the higher Mach number case, however, a large central region in the late time plot shows no clear state of correlation. This is not found in the lower Mach number plot. Recall that the level of correlation is less for the higher Mach number cases at any given time (Figure 5a). At  $t = 1$ , Mach number variation of  $\chi$  is only evident in the short wavelength regime. This regime is somewhat more negative for the low  $M$  run. However, at  $t = 5$ , the spectra exhibit differences at large and small scales. The tendency toward bifurcation is clear by now, but domination by one sign of cross helicity is not as pronounced at short wavelengths for  $M = 0.6$ . At  $t = 10$ , the spectra of magnetic and velocity fields in very low and very high wavenumber regions are correlated, but wavenumbers in the middle range are in a mixed state of correlation. Note that total bifurcation is episodic for both cases, *e.g.*, Figure 17a indicates that the  $M = 0.2$  case has become bipolar at  $t = 5$ , however, at  $t = 10$  there is no sharp break between region of oppositely signed normalized cross helicity. Numerical simulations out to larger times are required to see if these systems settle into a completely bifurcated state.

These simulations do show, however, that the details of normalized cross helicity transfer are sensitive to the degree of compressibility of the turbulent magnetofluid.

#### IV. CONCLUSIONS

To determine the effects of compressibility on the phenomenology of MHD turbulence, we have taken the direct approach of choosing a simple, though nontrivial, test problem which has a well-known incompressible MHD evolution. Although this choice of initial conditions might limit the phase space accessible to the compressible system, it does permit a direct comparison of the evolution of turbulence in the two cases and results in the identification of specific compressible effects. The present calculations have concentrated on initially average subsonic flows and have permitted  $\beta$  to change inversely with Mach number. Another approach which we are presently investigating is to maintain  $\beta$  at a constant value and vary the Mach number by varying the initial mass density. The use of variable mass density permits a wider range of Mach numbers to be considered, including the supersonic regime.

In this paper we have investigated the dynamic evolution of compressible magnetofluids as a function of initial average Mach number, in terms of global quantities, flow morphology, and spectra. Perhaps the most theoretically meaningful quantities chosen for comparison are the global quantities. Comparison of global quantities shows that some differences in evolution can be described in terms of initial average Mach number. These results also show that no sudden qualitative changes in behavior occur for the range of initial average Mach numbers studied, but rather a slow progression. Our calculations thus indicate that, to some extent, observations of compressible magnetohydrodynamic turbulence can be interpreted in terms of incompressible MHD turbulence theory for Mach numbers less than about one. The relevance of incompressible MHD turbulence theory to supersonic systems remains to be tested. Dynamic alignment occurs in compressible as well as in incompressible media; system evolution and the physics of reconnection are similar, excluding variations in the mass density and temperature. The alignment measures

of  $\mathbf{v}$  and  $\mathbf{B}$  decrease at a given time as Mach number increases, so that compressibility retards or limits the process for the Orszag-Tang vortex. The physics of selective decay as a function of  $M$  is significantly different when compared to the dependence on inverse dissipation, even though the alignment coefficients decrease with increasing Mach number, as with increasing Lundquist number. Some variables, such as average kinetic and magnetic energies and kinetic and magnetic enstrophies, show little variation over the range of Mach number we have studied. Note that we have drastically simplified the transport coefficients by assuming them to be isotropic and temperature independent. A more realistic treatment of transport might alter our conclusions somewhat. Note also that the behavior of ideal, incompressible global invariants is not identical in the two media. In the compressible medium these quantities often fluctuate around the normalized compressible analogs or behave in a manner that is qualitatively similar to the incompressible results.

Our second means of study is point-to-point local comparison of solutions as a function of Mach number. While the qualitative observations regarding common variables in the Orszag-Tang vortex, like the velocity and magnetic field, are similar, the details of the various phenomena differ in significant ways. Some features of compressible flows have no analog in incompressible media. This is true, for example, of compressible variations in mass density. The high density jets produced by magnetic reconnection are one important feature which the incompressible calculations cannot model or estimate. Another striking feature in direct solution comparison is the emergence of smaller scale rotational structure in the velocity field with increasing Mach number. The central large scale vortices appear to split into vortex pairs at high subsonic Mach numbers. Small scale structure also increases with higher Lundquist numbers as in incompressible flows but more so at higher  $M$ . The size of the Mach number relative to the Lundquist number should be important in this phenomenon, since the former is a measure of the magnitude of velocity fluctuations while the latter is a measure of the degree to which dissipation will reduce such fluctuations. The source term in the vorticity evolution equation for compressible flow (Eq. (12)) contributes to changes in the vorticity through pressure and density fluctuations [9], as well as by

altering the magnetic source term. These changes should translate into smaller scale structure in the flow field. Spectral plots as a function of  $M$  support this conclusion and hint that compressibility might significantly alter spectral transfer in the inertial range.

None of the above results have depended explicitly upon the feature usually associated with compressible flows—finite sound waves and shock waves. We saw little direct evidence of such waves in our calculations. This will be the subject of our next paper on the supersonic regime. Our earlier results [19], combined with those of Passot and Pouquet, indicate that novel phenomena occur when compressible initial conditions are used. However, we point out that, in a region containing shocks and for which  $\langle v \rangle = 0$ , the flows will be subsonic in the portions bounded by shocks, so that the conclusions that we have reached here will be important to the case of supersonic flow as well.

#### ACKNOWLEDGEMENTS

The authors thank J. P. Dahlburg and S. G. Lambrakos for helpful discussions. We also thank J. H. Gardner, J. T. Mariska, and J. T. Karpen for comments on the manuscript. The numerical simulations reported here were performed on the NASA Ames Research Center Cray-2 supercomputers and on the NRL Cray-XMP/24. This work was supported by the NASA Solar Terrestrial Theory Program and the Office of Naval Research.



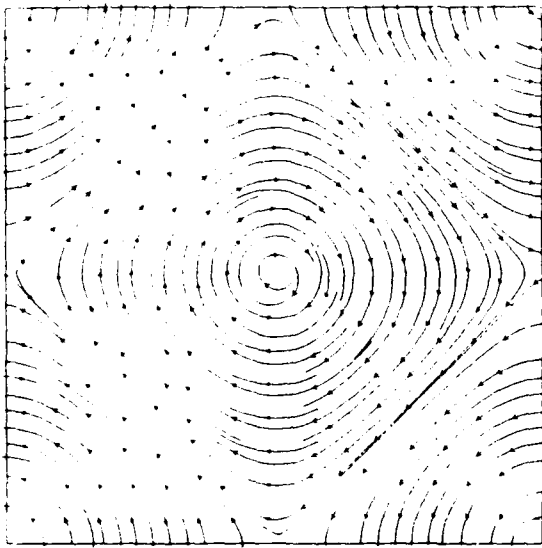
## References

1. D. Montgomery and L. Phillips, *Phys. Rev. A* **38**(6), 2953 (1988)
2. E. Marsch and A. Mangeney, *J. Geophys. Res.* **92**(A7), 7363 (1987).
3. L. Ting, *Phys. Fluids* **17**(8), 1518 (1974).
4. T. A. Zang, M. Y. Hussaini, and D. M. Bushnell, *AIAA J.* **22**, 13 (1984).
5. H. S. Ribner, *AIAA J.* **25**(3), 436 (1987).
6. M. J. Lighthill, *Proc. Roy. Soc. A* **211**, 564 (1952).
7. M. J. Lighthill, *Proc. Roy. Soc. A* **222**, 1 (1954).
8. J. M. Picone, J. P. Boris, J. R. Greig, M. Raleigh, and R. F. Fernsler, *J. Atmos. Sci.* **38**(9), 2056 (1981).
9. J. M. Picone and J. P. Boris, *Phys. Fluids* **26**(2), 365 (1983).
10. J. M. Picone and J. P. Boris, *J. Fluid Mech.* **189**, 23 (1988).
11. J. M. Picone and J. P. Boris, in *Proceedings of the International Workshop on compressible Turbulent Mixing*, ed. by A. Buckingham (Springer-Verlag, New York, 1989), to be published.
12. A. S. Monin and A. M. Yaglom, *Statistical Fluid Mechanics, Vol. 2* (MIT Press, Boston, 1975), Section 20.
13. L. M. Milne-Thomson, *Theoretical Hydrodynamics* (Macmillan, New York, 1968), Chapter 13.
14. D. Montgomery, M. R. Brown, and W. H. Matthaeus, *J. Geophys. Res.* **92**(A1), 282 (1987).
15. J. V. Shebalin and D. Montgomery, *J. Plasma Phys.* **39**(2), 339 (1988).
16. S. S. Moiseev, V. I. Petviashvily, A. V. Toor, and V. V. Yanovsky, *Physica 2D*, 218 (1981).

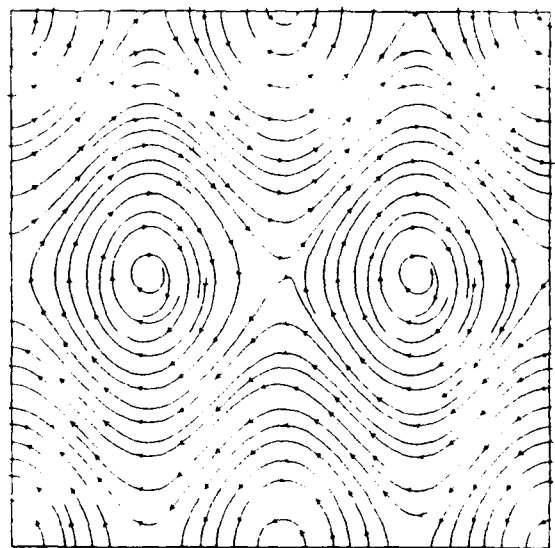
17. T. Passot and A. Pouquet, *J. Fluid Mech.* **181**, 441 (1987).
18. G. Erlebacher, M. Y. Hussaini, C. G. Speziale, and T. A. Zang, *ICASE Report 87-20* (1987).
19. R. B. Dahlburg, J. M. Picone, and J. T. Karpen, *J. Geophys. Res.* **93**(A4), 2527 (1988).
20. R. Horiuchi and T. Sato, *Phys. Fluids* **29** (12), 4174 (1986).
21. R. Horiuchi and T. Sato, *Phys. Fluids* **31**(5), 1142 (1988).
22. S. Riyopoulos, A. Bondeson, and D. Montgomery, *Phys. Fluids* **25**, 107 (1982).
23. S. A. Orszag and C.-M. Tang, *J. Fluid Mech.* **90**, 129 (1979).
24. J. Léorat, R. Grappin, A. Pouquet, and U. Frisch, in *Stellar and Planetary Magnetism*, ed. by A. M. Soward (Gordon and Breach, New York, 1983).
25. U. Frisch, A. Pouquet, P. -L. Sulem, and M. Meneguzzi *J. Mec. Theor. Appl. Numero Special*, 191 (1983).
26. A. Pouquet, M. Meneguzzi, and U. Frisch, *Physical Review A* **33**(6), 4266 (1986).
27. P. L. Sulem, A. Pouquet, and M. Meneguzzi, in *Advances in Turbulence*, ed. by G. Comte-Bellot and J. Mathieu (Springer-Verlag, New York, 1987).
28. A. Pouquet, P. -L. Sulem, and M. Meneguzzi, *Phys. Fluids* **31**, 2635 (1988).
29. D. Fyfe and D. Montgomery, *J. Plasma Phys.* **16**, 181 (1976).
30. D. Fyfe, G. Joyce, and D. Montgomery, *J. Plasma Phys.* **17**, 317 (1977).
31. D. Fyfe, D. Montgomery, and G. Joyce *J. Plasma Phys.* **17**, 369 (1977).
32. R. Kraichnan D. Montgomery, *Rep. Prog. Phys.* **43**, 547 (1980).
33. W. H. Matthaeus and D. Montgomery, *Ann. N. Y. Acad. Sci.* **357**, 203 (1980).

34. R. B. Dahlburg, J. M. Picone, and J. T. Karpen, *Outstanding Problems in Solar System Plasma Physics 1988*, ed. J. L. Burch and J. H. Waite, AGU, Washington D. C. (1989), in press.
35. R. Peyret and T. D. Taylor, *Computational Methods for Fluid Flow* (Springer-Verlag, New York, 1983).
36. R. B. Dahlburg, T. A. Zang, D. Montgomery, and M. Y. Hussaini, *Proc. Nat. Acad. Sci. USA* **80**, 5798 (1983).
37. D. D. Schnack, D. C. Barnes, Z. Mikić, D. S. Harned, E. J. Caramana, and R. A. Nebel, *Computer Phys. Commun.* **43**, 17 (1986).
38. Z. Mikić, D. C. Barnes, and D. D. Schnack, *Ap. J.* **328**, 830 (1988).
39. R. Courant and K. O. Friedrichs, *Supersonic Flow and Shock Waves* (Springer-Verlag, New York, 1977)
40. P. J. Roache, *Computational Fluid Dynamics* (Hermosa Publishers, Albuquerque, 1976), 222, and references therein.
41. G. Patnaik, R. H. Guirguis, J. P. Boris, and E. S. Oran, *J. Comp. Phys.* **71**, 1 (1987).
42. C. Canuto, M. Y. Hussaini, A. Quarteroni, and T. A. Zang, *Spectral Methods in Fluid Dynamics* (Springer-Verlag, New York, 1988).
43. W. S. Dorn and D. D. McCracken, *Numerical Methods with FORTRAN IV Case Studies* (John Wiley & Sons, New York, 1972), 369.
44. C. R. Evans and J. F. Hawley, *Ap. J.* **332**, 659 (1988).
45. C. H. Finan III and J. Killeen, *Computer Phys. Commun.* **24**, 441 (1981).
46. R. B. Dahlburg, J. P. Dahlburg, and J. T. Mariska, *Astron. Astrophys.* **198**, 300 (1988).
47. R. B. Dahlburg, NRL Memo. Rep. 6012 (1987).

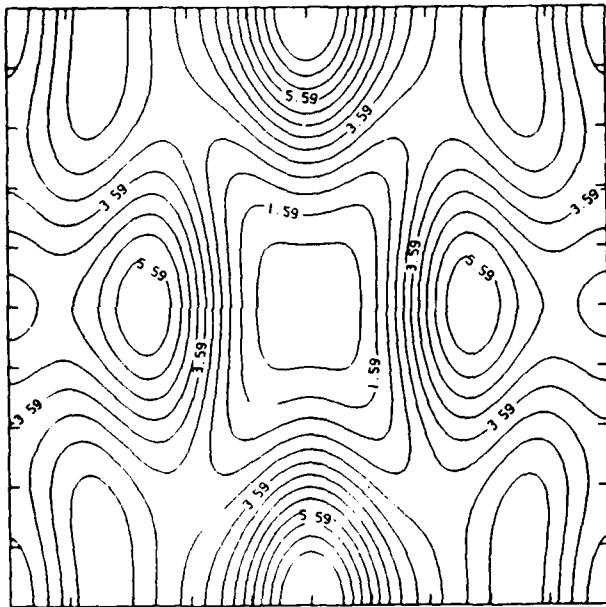
48. L. D. Landau and E. M. Lifshitz, *Fluid Mechanics* (Pergamon, New York, 1959), 322.
49. A. Hasegawa, *Adv. Phys.* **34**, 1 (1985)
50. W. H. Matthaeus, M. L. Goldstein, and D. C. Montgomery, *Phys. Rev. Lett.* **51**, 1484 (1983)
51. R. Grappin, *Phys. Fluids* **29**, 2433 (1986).
52. W. H. Matthaeus, *Geophys. Res. Lett.* **9**, 660 (1982).
53. R. B. Dahlburg, T. A. Zang, and D. Montgomery, *J. Fluid Mech.* **169**, 71 (1986).
54. W. H. Matthaeus and D. Montgomery, *J. Plasma Phys.* **25**, 11 (1981).



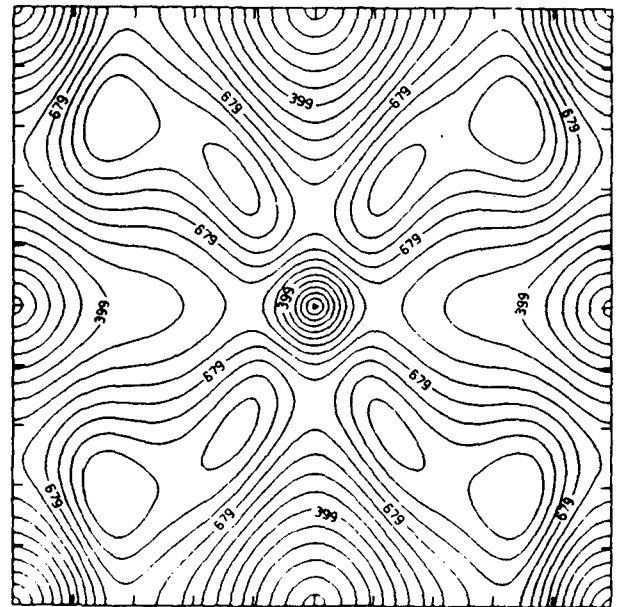
a.



b.



c.



d.

Figure 1. Initial conditions: a. velocity field; b. magnetic field; Initial conditions specific to the  $M = 0.6$  case: c. thermal pressure field; d. local Mach number. Minimum and maximum values are 0.73 and 7.9 for thermal pressure and 0.0 and 0.97 for local Mach number.

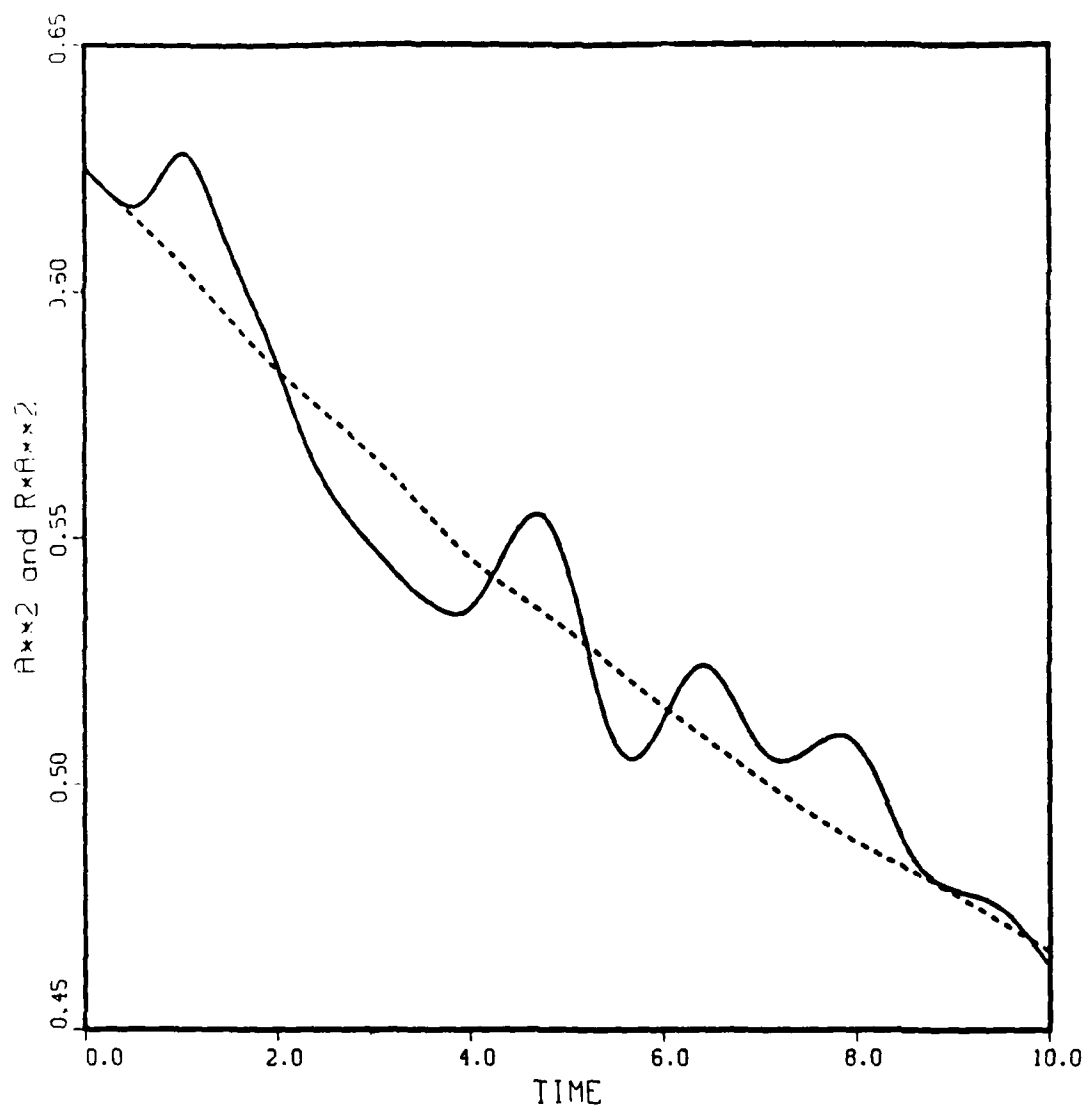
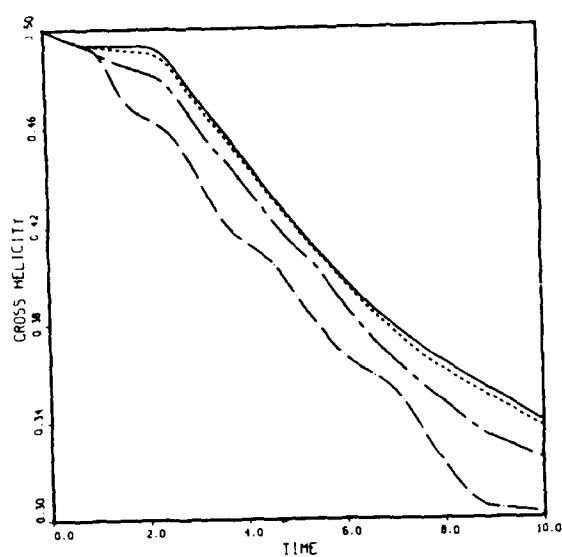
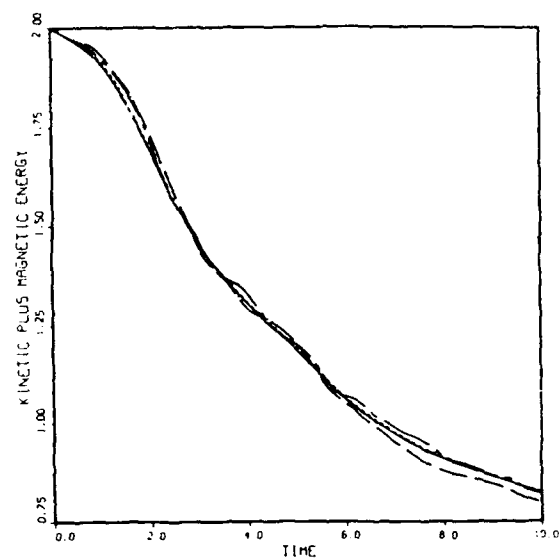


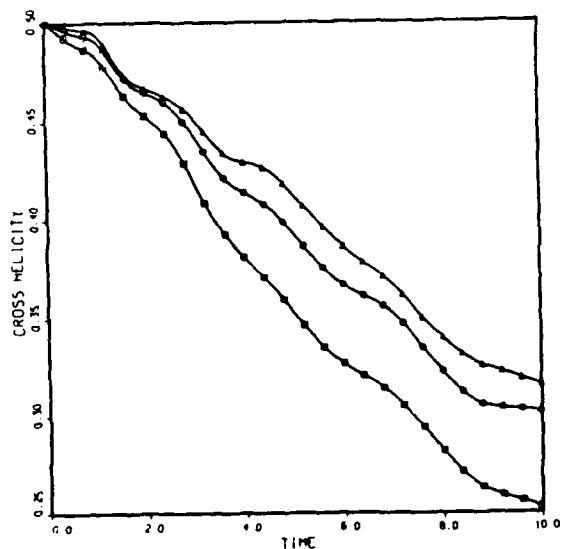
Figure 2. Time evolution of the mean square magnetic vector potential ( $\langle a^2 \rangle$  - solid line) and its compressible analogue ( $\langle \rho a^2 \rangle$  - dashed line), both for the compressible  $M = 0.6, S = 100$  run.



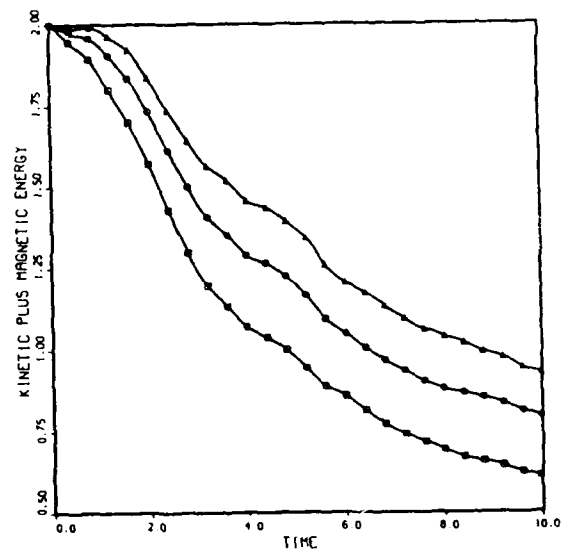
a.



b.

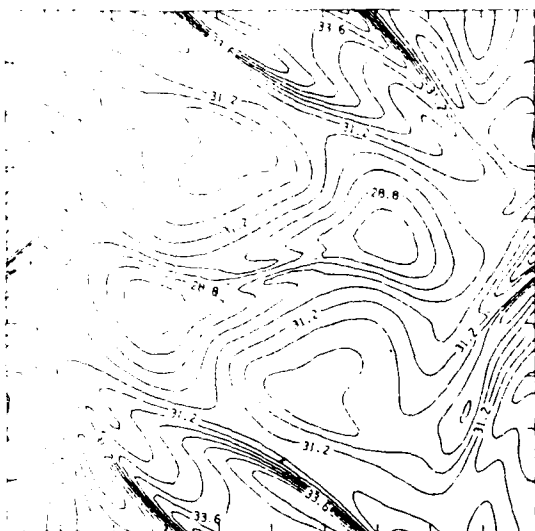


c.

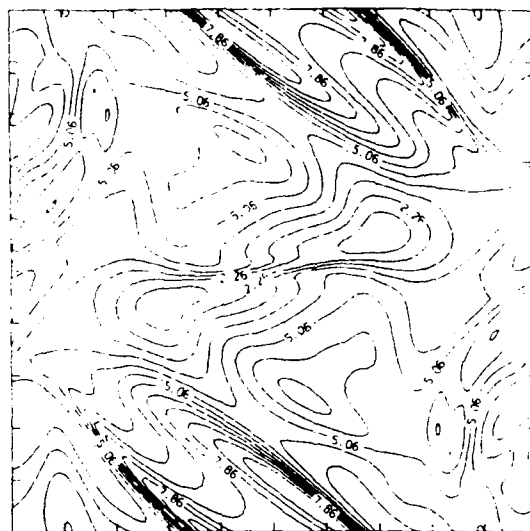


d.

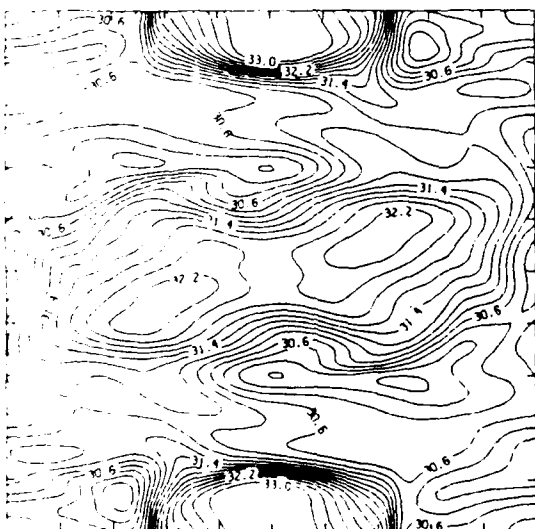
Figure 3. Variation of time evolution of global quantities parameterized by Mach number ( $M$ ) and by Lundquist number ( $S$ ): a. variation of cross helicity with  $M$  ( $S = 100$ ) (solid line—incompressible result, dashed line— $M = .2$ , mixed dashed line— $M = .4$ , and dash-dotted line— $M = .6$ ); b. variation of fluctuating energy (magnetic + kinetic) with  $M$ ; (figure key same as a); c. variation of cross helicity with  $S$  ( $M = .6$ ) (triangles— $S = 200$ , circles— $S = 100$ , and squares— $S = 50$ ); and d. variation of fluctuating energy (magnetic + kinetic) with  $S$  (figure key same as c).



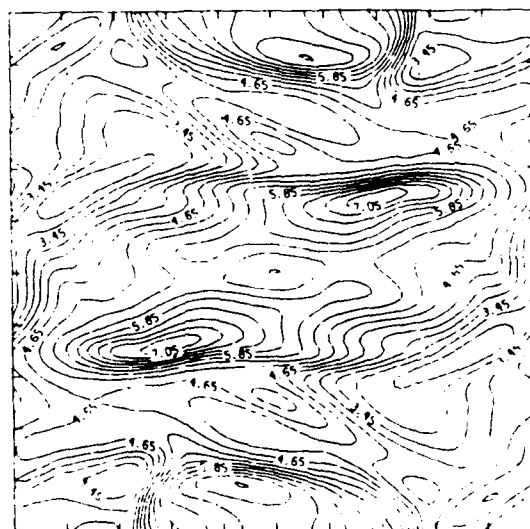
a.



b.



c.



d.

Figure 4. Contour plots of the polytropic coefficient for a.  $M = 0.2$  and b.  $M = 0.6$  at  $t = 2$ , and c.  $M = 0.2$  and b.  $M = 0.6$  at  $t = 8$ .  $S = 100$  for both cases. Minimum and maximum values are a. 27.8 and 35.4, b. 1.12 and 9.93, c. 29.8 and 33.3, and d. 2.62 and 7.29.



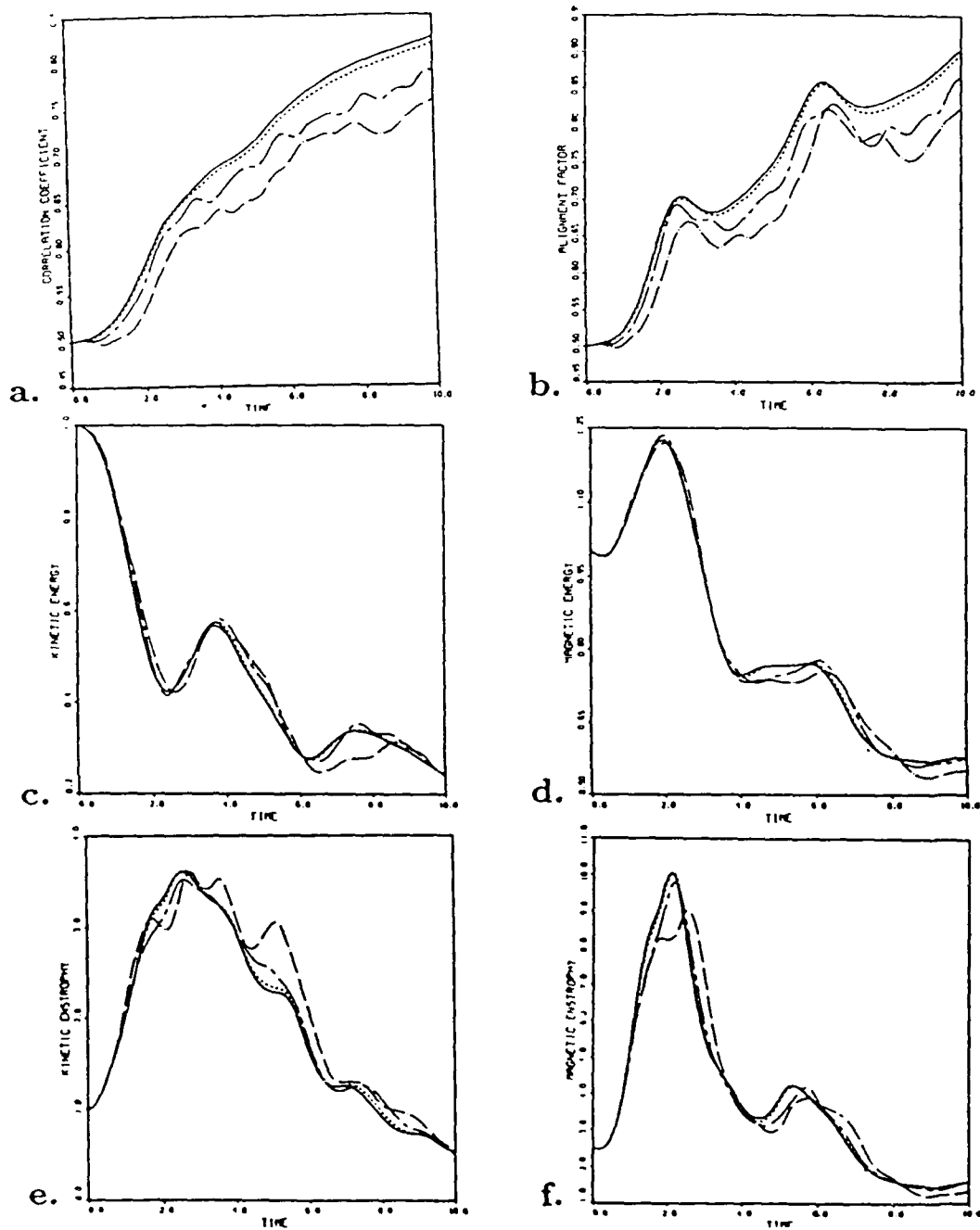
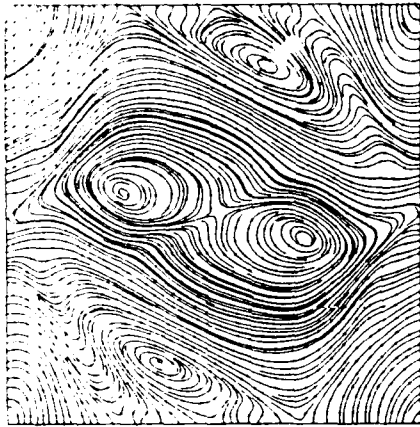
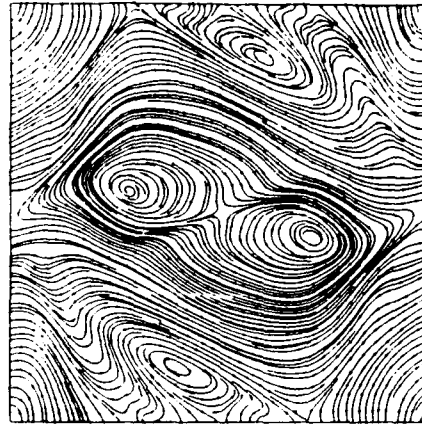


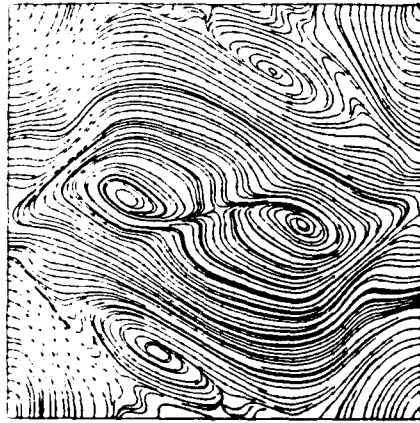
Figure 5. Variation of time evolution of global quantities parameterized by Mach number ( $M$ ),  $S = 100$  for all cases: (solid line—incompressible result, dashed line— $M = .2$ , mixed dashed line— $M = .4$ , and dash-dotted line— $M = .6$ ); a. correlation coefficient; b. alignment factor; c. kinetic energy; d. magnetic energy; e. kinetic enstrophy; and f. magnetic enstrophy.



a.



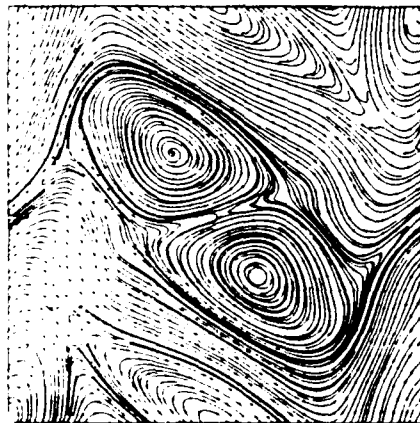
b.



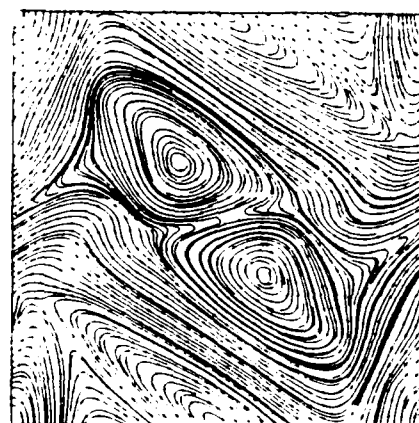
c.



d.

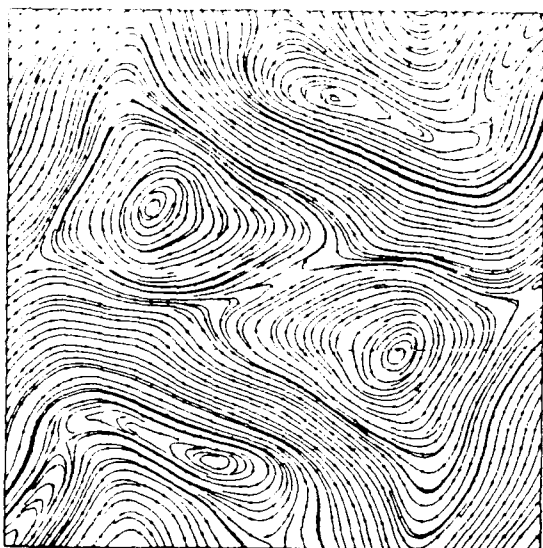


e.

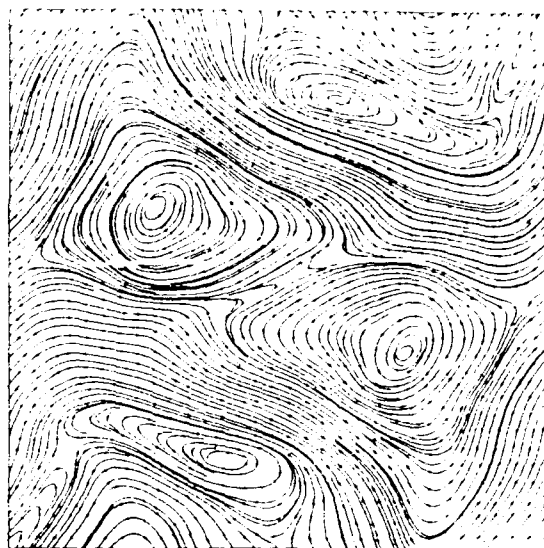


f.

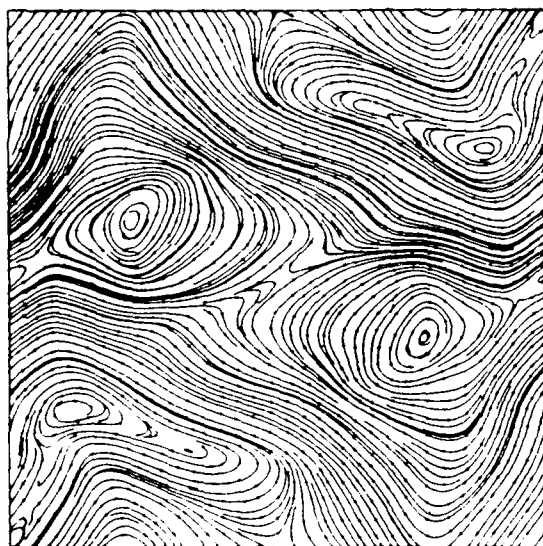
Figure 6. Variation of fields with Mach number ( $M$ ) at  $t = 2$  ( $S = 100$ ): a. velocity field (incompressible case); b. velocity field ( $M = 0.2$ ); c. velocity field ( $M = 0.4$ ); d. velocity field ( $M = 0.6$ ); e. magnetic field (incompressible case); and f. magnetic field ( $M = 0.6$ ).



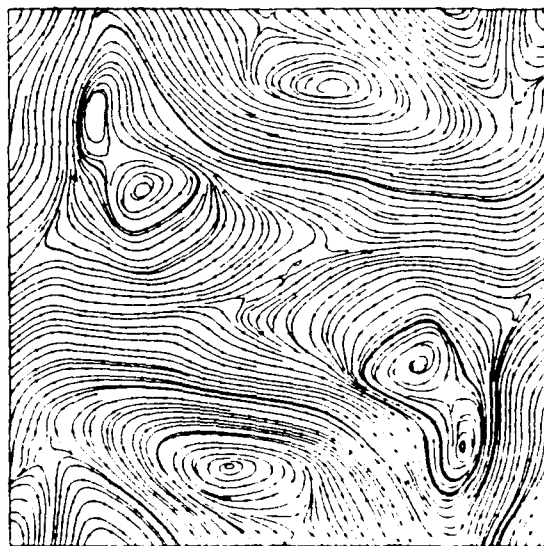
a.



b.

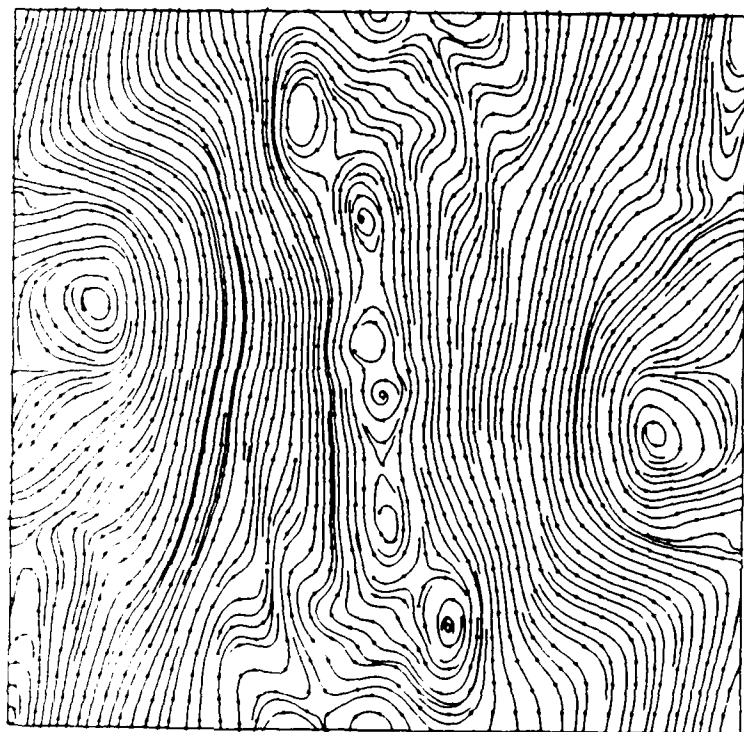


c.

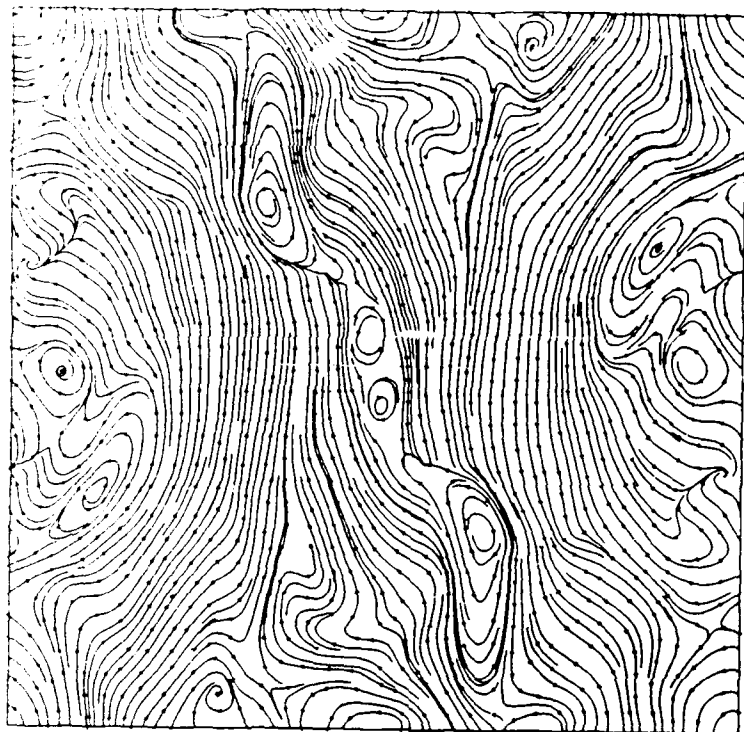


d.

Figure 7. Variation of velocity field with Mach number ( $M$ ) at  $t = 4$  ( $S = 100$ ): a. incompressible case; b.  $M = 0.2$ ; c.  $M = 0.4$ ; and d.  $M = 0.6$ .



**a.**



**b.**

Figure 8. Variation of velocity field at  $t = 8$  ( $S = 200$ ): a. incompressible case; and b.  
 $M = 0.6$ .

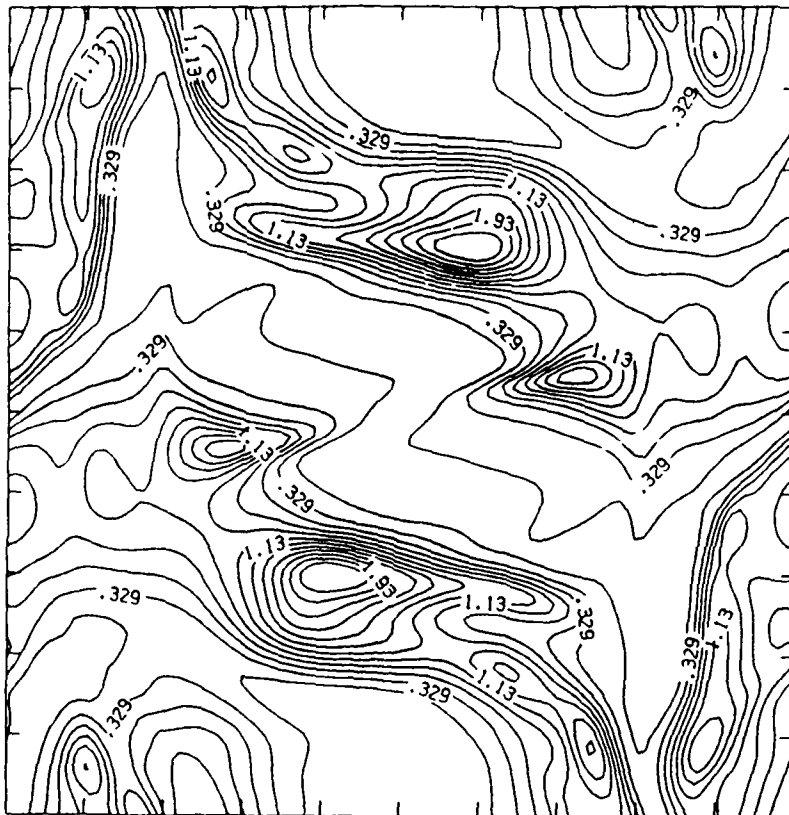
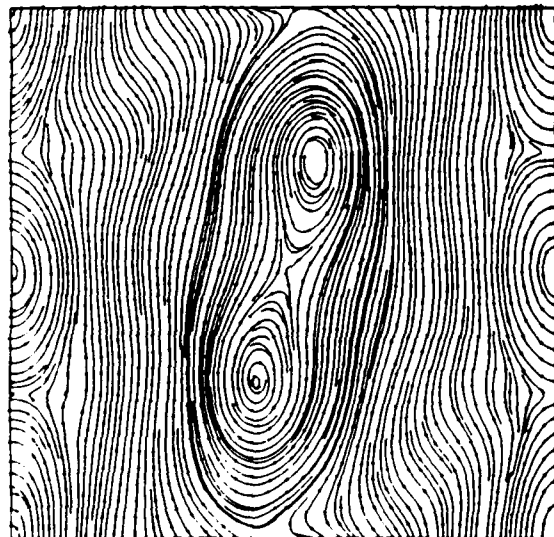
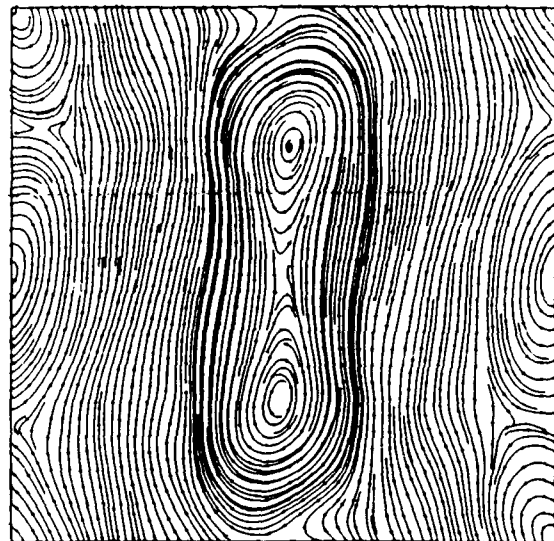


Figure 9. Contour plot of  $v^2$  at  $t = 4$  for  $M = 0.6$  and  $S = 100$ . Minimum and maximum values are 0.0 and 2.58.



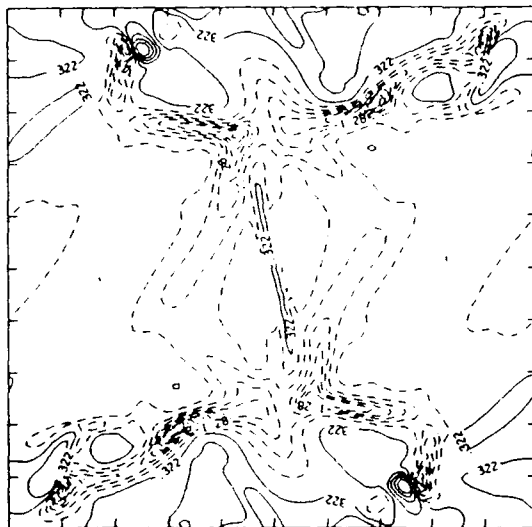
**a.**



**b.**

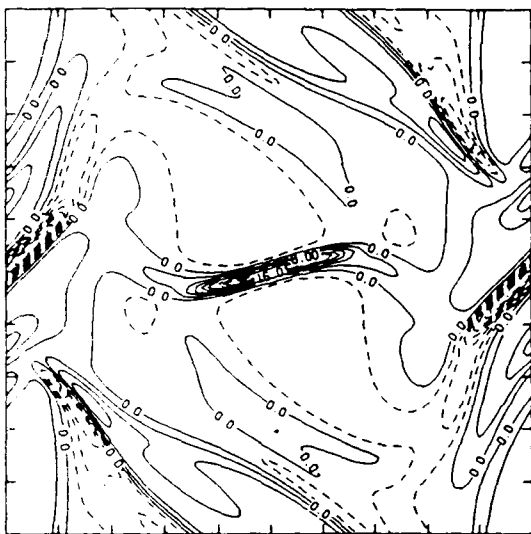
Figure 10. Variation of magnetic field at  $t = 8$  ( $S = 100$ ): a. incompressible case and b.

$$M = 0.6.$$

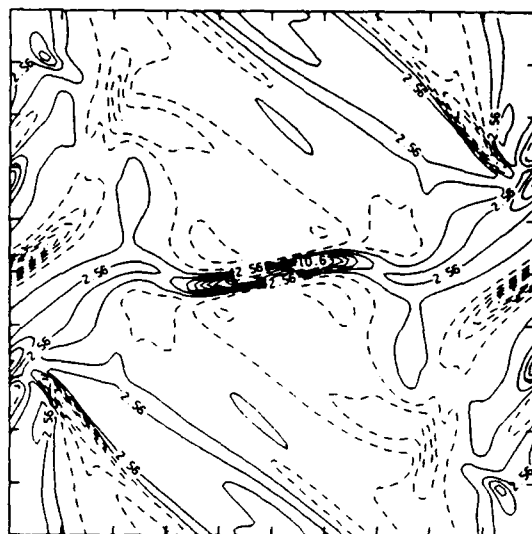


b.

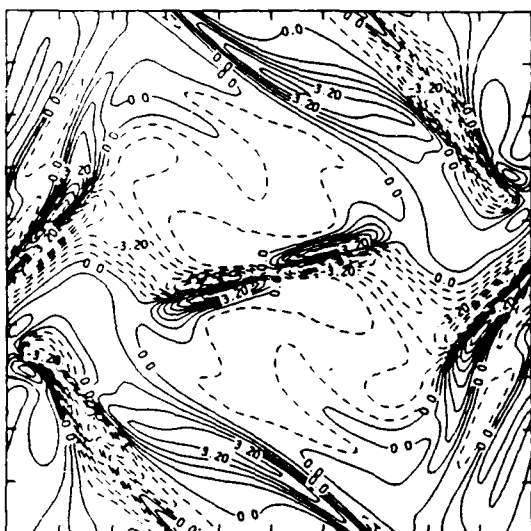
Figure 11. Variation of the local rate of dilatation as a function of Mach number  $M$  at  $t = 2$  ( $S = 100$ ); a.  $M = 0.2$  and b.  $M = 0.6$ . Minimum and maximum contour values are a. -0.107 and 0.104, and b. -4.01 and 2.58.



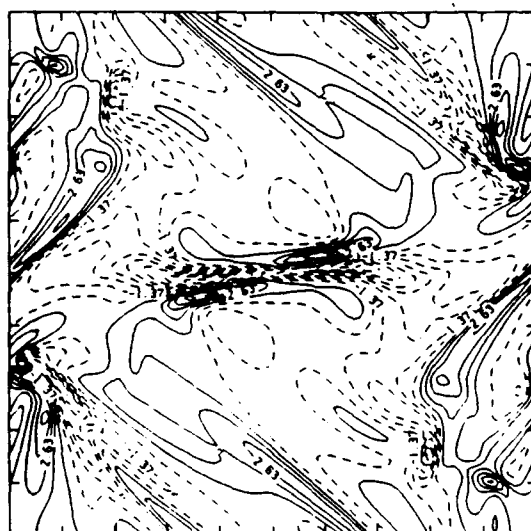
a.



b.



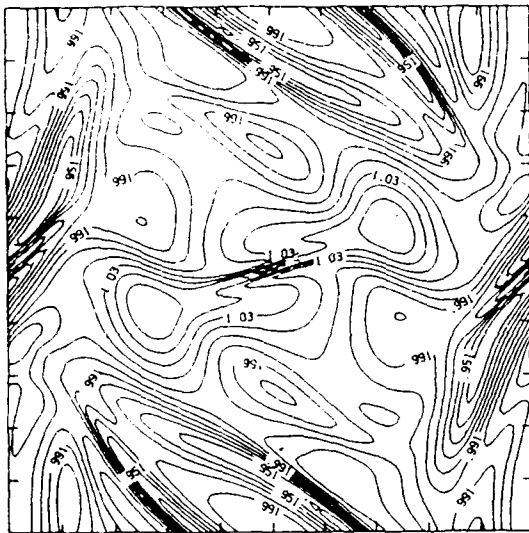
c.



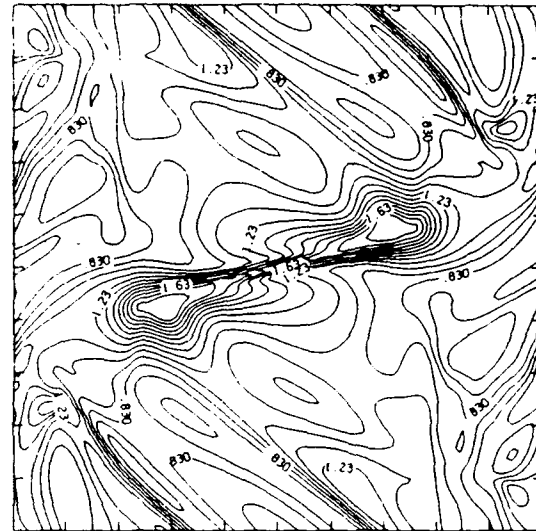
d.

Figure 12. Variation of fields at  $t = 2$  ( $S = 100$ ) a. electric current density (incompressible case); b. electric current density ( $M = 0.6$ ); c. vorticity (incompressible case); and d. vorticity ( $M = 0.6$ ). Minimum and maximum values are a. approximately -20.0 and 20.0, b. -13.1 and 20.4, c. approximately -6.40 and 6.40, and d. -8.10 and 6.45.

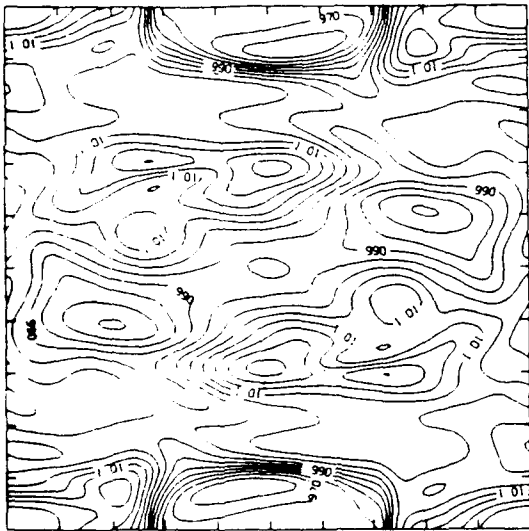




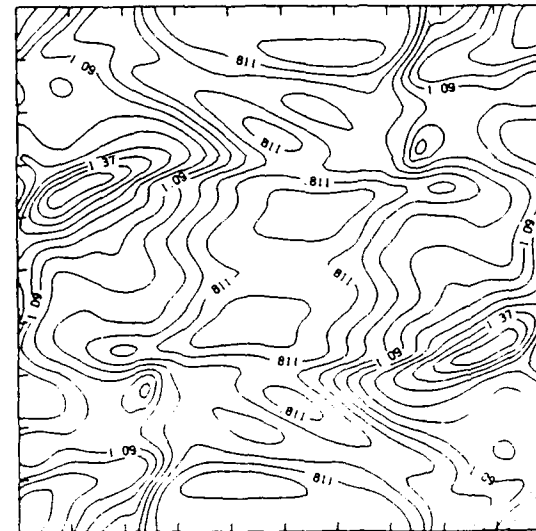
a.



b.



c.



d.

Figure 13. Variation of the mass density as a function of Mach number  $M$  ( $S = 100$ ) a.

$t = 2$  ( $M = 0.2$ ); b.  $t = 2$  ( $M = 0.6$ ); c.  $t = 8$  ( $M = 0.2$ ); and d.  $t = 8$  ( $M = 0.6$ ).

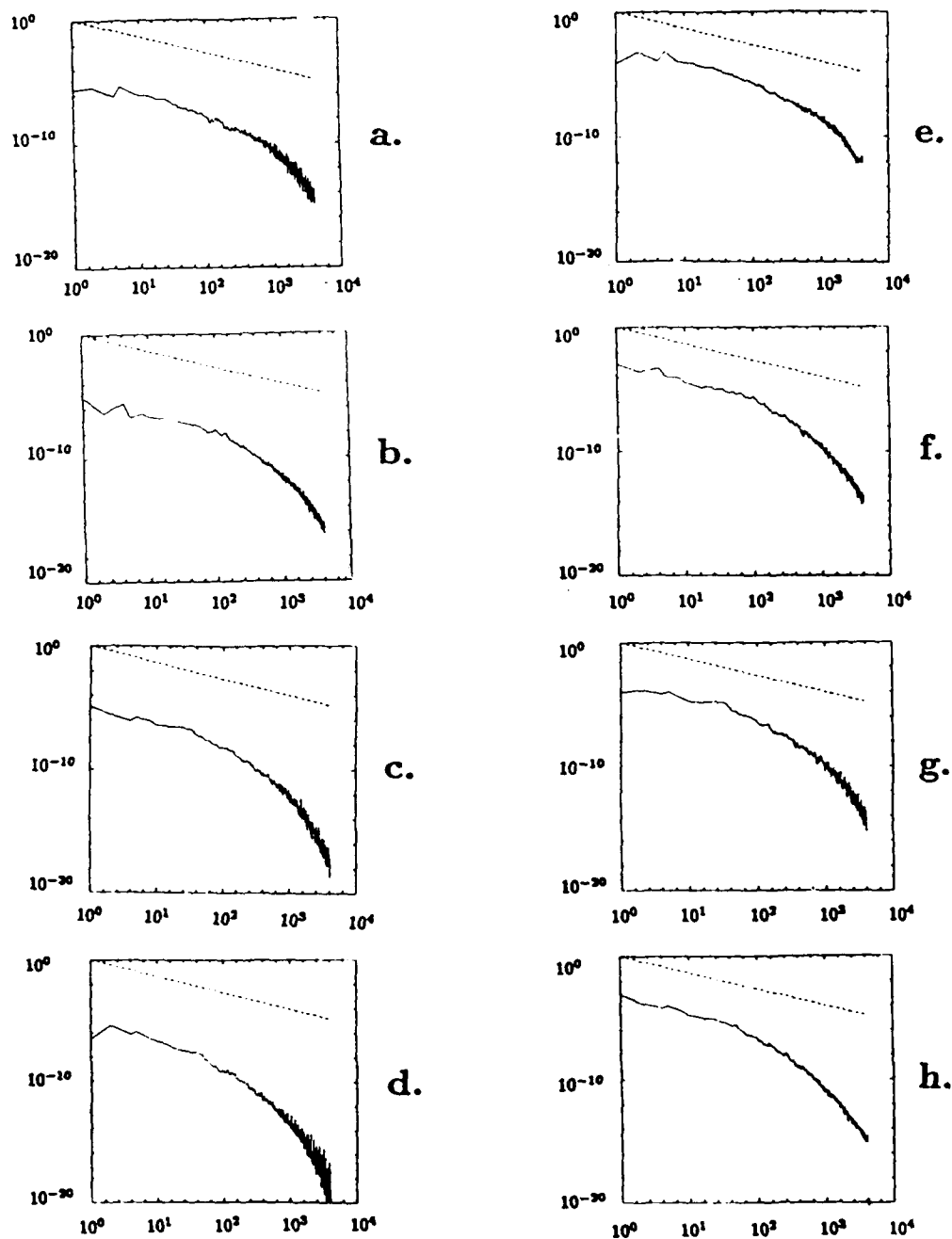


Figure 14. Spectral plots of the mass density:  $M = 0.2$  case at a.  $t = 2$ ; b.  $t = 4$ ; c.  $t = 6$ ; d.  $t = 8$ .  $M = 0.6$  case at e.  $t = 2$ ; f.  $t = 4$ ; g.  $t = 6$ ; h.  $t = 8$ .  $S = 100$  for all cases. The dashed line has a reference slope of  $-4/3$ .

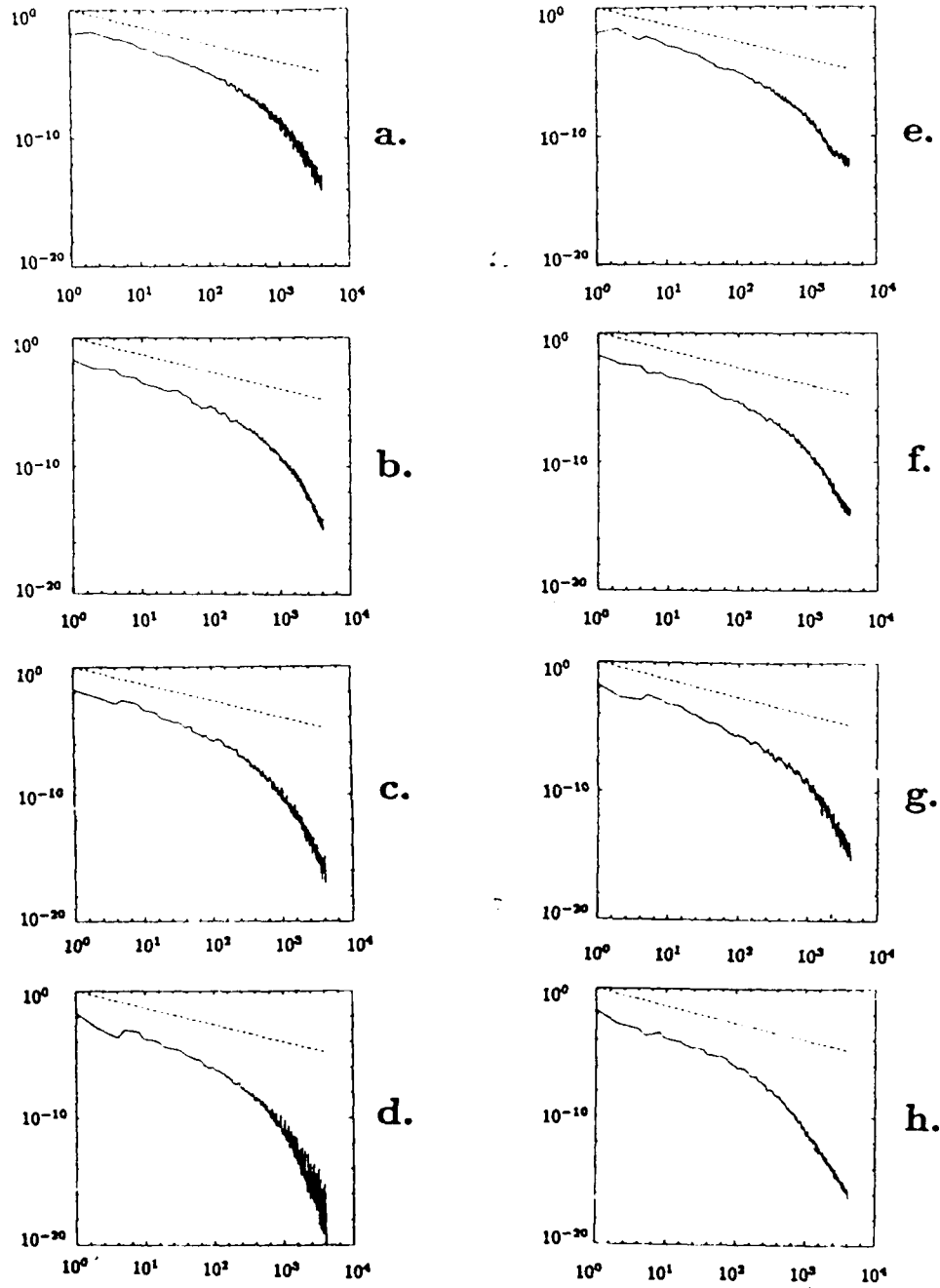


Figure 15. Spectral plots of the magnetic energy:  $M = 0.2$  case at a.  $t = 2$ ; b.  $t = 4$ ; c.  $t = 6$ ; d.  $t = 8$ .  $M = 0.6$  case at e.  $t = 2$ ; f.  $t = 4$ ; g.  $t = 6$ ; h.  $t = 8$ .  $S = 100$  for all cases. The dashed line has a reference slope of  $-4/3$ , corresponding to a  $k^{-5/3}$  omnidirectional energy spectrum.

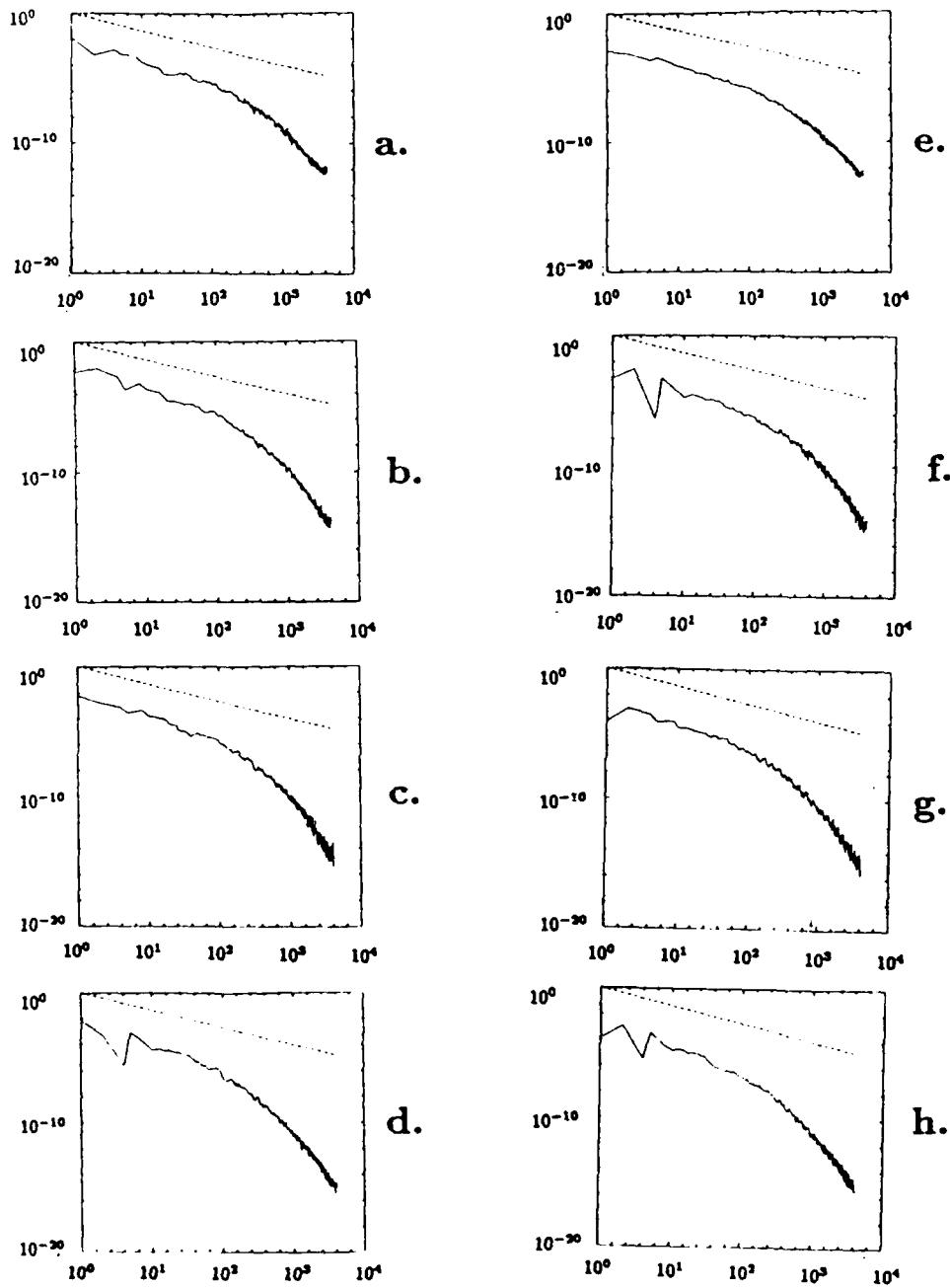
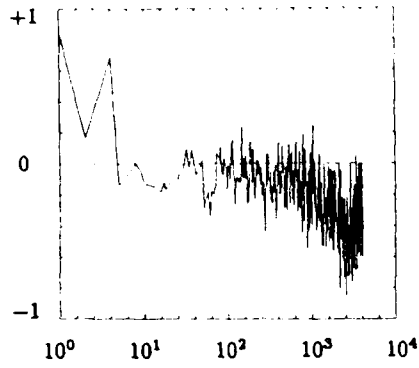
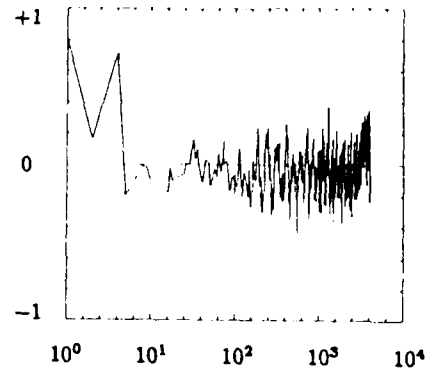


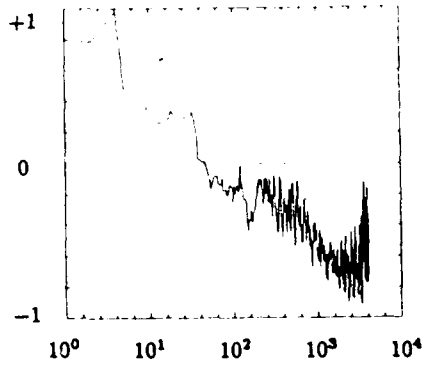
Figure 16. Spectral plots of the solenoidal and nonsolenoidal kinetic energy density for the  $M = 0.6$  case: solenoidal part at a.  $t = 2$ ; b.  $t = 4$ ; c.  $t = 6$ ; d.  $t = 8$ ; Nonsolenoidal part at e.  $t = 2$ ; f.  $t = 4$ ; g.  $t = 6$ ; h.  $t = 8$ .  $S = 100$  for all cases. The dashed line has a reference slope of  $-4/3$ .



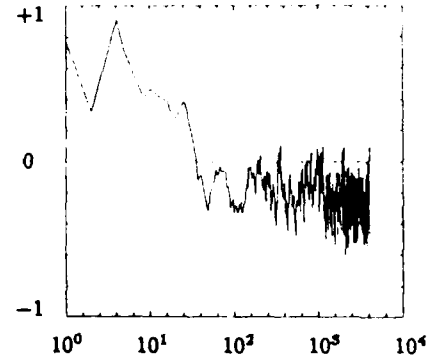
a.



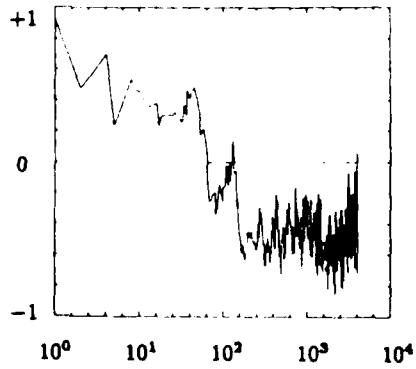
d.



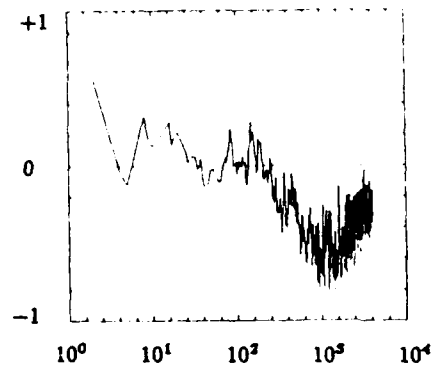
b.



e.



c.



f.

Figure 17. Spectral plots of the normalized cross-helicity:  $M = 0.2$  case at a.  $t = 1$ ; b.  $t = 5$ ; c.  $t = 10$ ;  $M = 0.6$  case at d.  $t = 1$ ; e.  $t = 5$ ; f.  $t = 10$ .  $S = 100$  for all cases. The dashed line has the reference value zero.